

NASA TM X-784

FACILITY FORM 602

N66 33307

(ACCESSION NUMBER)

72

(PAGES)

TMX-784

(NASA CR OR TMX OR AD NUMBER)

(THRU)

(CODE)

(CATEGORY)

33

NASA TM X-784

GPO PRICE \$

CFSTI PRICE(S) \$

Hard copy (HC)

Microfiche (MF)

W 653 July 65

TECHNICAL MEMORANDUM

X-784

PRELIMINARY EVALUATION OF A NUMBER OF ABLATIVE
HEAT-SHIELD MATERIALS EXPOSED TO COMBINED
RADIATIVE AND CONVECTIVE HEATING

By Robert R. Dickey and Jack F. Haacker

Ames Research Center
Moffett Field, Calif.

REMOVED FROM CATEGORY 7

AUTHORITY- MEMO FROM

DROBKA TO LEBOW DATED JUN 9 1966

DECLASSIFIED- AUTHORITY

US: 1286

DROBKA TO LEBOW

MEMO DATED

6/8/66

Declassified by authority of NASA
Classification Change Notices No. 67

Dated 11-6/29/66

NATIONAL AERONAUTICS AND SPACE ADMINISTRATION

WASHINGTON

March 1963

DECLASSIFIED

NATIONAL AERONAUTICS AND SPACE ADMINISTRATION

TECHNICAL MEMORANDUM X-784

PRELIMINARY EVALUATION OF A NUMBER OF ABLATIVE
HEAT-SHIELD MATERIALS EXPOSED TO COMBINED
RADIATIVE AND CONVECTIVE HEATING*

By Robert R. Dickey and Jack F. Haacker

SUMMARY

33307

Forty-six ablative heat-shield materials were tested at combined radiative and convective heat fluxes representative of the maximum stagnation point heat fluxes expected for a manned lifting-type vehicle entering the earth's atmosphere at escape velocity. These tests were made to determine which materials would be the most promising for more detailed studies to provide specific design data. Data obtained during the tests included time histories of the temperature at the back surface of each material, measurements of the amount of material ablated, and photographs of the ablated surface.

The materials were evaluated on the basis of the maximum temperature rise measured at the back surface of a sample of given weight per unit area (4.7 pounds per square foot). Balsa wood and cork had the lowest back-surface temperature rise; and insulating plaster, oak wood, and a group of plastic materials had the next lowest. Approximately half the materials tested appeared to be unsuitable for heat shields at the imposed heating rates because of their relatively high back-surface temperature rise.

Authoe

INTRODUCTION

Recent successful entries of earth orbiting capsules protected by heat shields of reinforced plastics have demonstrated the effectiveness of the ablative type of thermal protection system for entry at satellite speed, where the heating is primarily convective. For entry at the greater speeds associated with lunar missions, the stagnation point region of a blunt capsule is heated by radiative as well as convective heat flux. Consequently, the question arises as to the possible effects of radiative heating on the performance of ablative heat-shield materials.

*Title, Unclassified

[REDACTED]

03710201030

Since the majority of the data on the effectiveness of ablative materials has been obtained under conditions of convective heating only, the present investigation was initiated to obtain data at the combined maximum radiative and convective heating rates expected at the stagnation point of a manned lunar vehicle. A large number of materials were evaluated on the basis of the maximum temperature rise measured at the back surface of a sample of a given weight per unit area. Supplementary data obtained included measurements of the amounts of material ablated, post-run photographs of the ablated surfaces, and photographs of the model profiles before and after testing.

NOTATION

A	area, ft ²
A/A*	nozzle area ratio
c _p	specific heat, Btu/lb-°F
H _{eff}	effective heat of ablation, Btu/lb
h	enthalpy, Btu/lb
K	thermal conductivity, Btu/ft ² /sec/°F/ft
M	Mach number
m	mass, lb
Δm	mass loss, lb
p	pressure, atm
Q	total heat, Btu
q _c	convective heating rate, Btu/ft ² -sec
q _r	radiative heating rate, Btu/ft ² -sec
R	nose radius, in.
Re	Reynolds number based on nose radius
T	temperature, °F
T _a	ablation temperature, °F
T _o	room temperature, °F
ΔT	temperature rise, (T-T _o), °F

DECLASSIFIED

t time, sec
w weight per unit area, lb/ft²
ρ density, lb/ft³

Subscripts

c convective heating
i initial
n nonstandard core weight
r radiative heating
s standard core weight
t total
max maximum
1 conditions ahead of normal shock
2 conditions behind normal shock

TEST FACILITY

The tests were conducted in the Ames entry heating simulator which is a facility capable of simultaneously simulating both the convective and radiative heating fluxes encountered by entry vehicles. The facility, which is illustrated schematically in figure 1, consists of a supersonic wind tunnel employing arc-heated air to produce the convective heating flux and a carbon arc to provide the radiative flux. A photograph of the entry heating simulator is shown in figure 2. The facility is described in detail in reference 1. Brief descriptions of the convective and radiative components are given below.

Convective Heating System

A schematic drawing of the arc-type air heater is shown in figure 3. Air from high-pressure storage tanks is introduced into the arc chamber where it is heated by a direct-current arc discharge between two concentric, water-cooled, ring-shaped, copper electrodes. A magnetic field at right angles to the arc discharge moves the arc around the gap between the electrode rings. This rotation of the arc minimizes the ablation of the copper electrodes and the consequent contamination of the air stream. The temperature rise in the uncooled

03712001030

parts of the air heater limits its operating time to less than 30 seconds duration. After being heated by the arc, the air is expanded through a supersonic nozzle into the test chamber as a free jet and then exhausted into a large evacuated sphere. The nozzle used during this investigation had an exit diameter of 2.28 inches and an A/A^* ratio of 13.00. A more detailed discussion of the design and performance characteristics of the arc heater and supersonic jet may be found in references 2 and 3.

Radiative Heating System

The radiative heating flux is supplied by a carbon arc which operates at atmospheric pressure and is separated from the test chamber by a quartz window (see fig. 1). The arc is positioned at the focal point of an ellipsoidal primary mirror. Energy from the arc is reflected by the primary mirror through the quartz window to the ellipsoidal secondary mirror where it is refocused onto the model. The magnitude of the radiative flux impinging on the model is controlled by wire screens of different porosity placed in front of the quartz window. A pneumatically operated shutter is used to synchronize the duration of the radiative flux with that of the convective flux. The carbon arc used in these tests has a spectral distribution in the ultraviolet region that closely simulates the spectrum of shock-heated air at temperatures and densities representative of entry at escape velocity of a lifting manned vehicle. However, (as shown in ref. 1) at wavelengths above approximately 4500 angstroms, the output intensity of the arc is greater than that calculated for shock-heated air. The effect of the quartz window and the wire screens on the spectral distribution is believed to be small.

MODELS

Two types of models were employed: ablation models were used to measure the relative performance of the various materials, and a calorimeter model was used to measure coldwall heat-transfer rates. Dimensioned drawings of the two types of models are shown in figure 4.

The ablation models were hemisphere-cylinders. (See fig. 4(a).) Each was constructed of two parts; a center test core and a concentric outer shell which served as a shroud and support for the test core. The test core was inserted into the shroud with a press fit and, except where noted, the shroud and core were constructed of the same test material. A thermocouple was embedded and glued into the base of each test core and a radiation shield was interposed between the core and the inner wall of the shroud to prevent the shroud from radiating heat to the core or the thermocouple.

Since the materials were to be compared on the basis of equal-weight per unit area, it was necessary to vary the core lengths inversely with the densities of the materials. The initial core weight of all materials (with two exceptions

which will be discussed later) was 0.00250 ± 0.00002 pound which corresponds to core lengths of 0.4 to 1.5 inches and a weight per unit area of 4.7 pounds per square foot.

The calorimeter model (fig. 4(b)) consisted of a copper slug, with a thermocouple embedded in the base, and a concentric outer shroud. The slug was supported within the shroud by small pointed pins to minimize conduction losses. Except for the small air gap between the calorimeter slug and shroud, the external shape and dimensions of the calorimeter model were the same as those of the ablation models.

TEST CONDITIONS AND PROCEDURES

All of the materials were tested at the following nominal conditions:

Convective heat-transfer rate, \dot{q}_c , Btu/ft ² -sec	230
Radiative heat-transfer rate, \dot{q}_r , Btu/ft ² -sec	140
Duration of heat pulse, t , sec	15
Total convective heat, Q_c , Btu/ft ²	3450
Total radiative heat, Q_r , Btu/ft ²	2100
Stagnation enthalpy, h_t , Btu/lb	4250
Free-stream total pressure, p_{t1} , atm	1/4
Stagnation pressure, p_{t2} , atm	1/32
Air mass flow, \dot{m} , lb/sec	0.0080
Mach number, M	3.8
Nozzle area ratio, A/A^*	13
Reynolds number based on nose radius, Re	100

The stagnation enthalpy of the arc-heated air was determined by the equilibrium sonic-flow method described in reference 1. Variations in the operation of the arc unit resulted in deviations of ± 250 Btu/lb from the nominal stagnation enthalpy value.

The output from the thermocouple located at the back surface of each test specimen was measured with a high-sensitivity galvanometer and recorded on an oscillograph during both the heating period of 15 seconds and a subsequent "soaking" period of several minutes after the heat pulse ended. During the "soaking" period, there was no air flow over the model and the pressure in the test chamber was approximately 200 to 400 microns of mercury. The maximum back-surface temperature rise during the heating and soaking periods was determined from the oscillograph trace.

The heat flow in the stagnation region of a large blunt heat shield is essentially one-dimensional. Preliminary tests had indicated that to achieve one-dimensional heat flow in small ablation models, great care must be exercised in designing the models. The particular model design employed during these tests was chosen in an attempt to minimize the heat flow into or out of the test core from regions other than the stagnation-point region. To determine whether the heat flow in the test cores was essentially one-dimensional, the maximum

back-surface temperature rise of one particular material (white Teflon) was measured at several different convective heating rates and compared with the theoretical variation of temperature rise with heating rate for one-dimensional heat flow (calculated from the theory of ref. 4). The results are shown in figure 5. The agreement between the measured and theoretical temperature rises indicates that the heat flow in the Teflon test cores was one-dimensional. White Teflon was used for the foregoing comparison because the ablation processes of a subliming material, such as Teflon, are less complex than those of a charring ablator and because data concerning the thermal characteristics of Teflon were readily available.

In addition to the time histories of the back-surface temperature, the data obtained during this investigation included the weights of the test cores before and after testing, post-run photographs of the ablated surfaces, and photographs of the model profiles before and after testing.

Cold-wall heat-transfer rates were measured at frequent intervals during the test program with the calorimeter described previously. The output from the calorimeter thermocouple was recorded on an oscillograph and the heat-transfer rate calculated from the relation

$$\dot{q} = \frac{mc_p}{A} \frac{dT}{dt}$$

where m and A are the mass and the front surface area of the calorimeter slug, c_p is the specific heat of the calorimeter slug, and dT/dt is the measured slope of the temperature versus time curve determined from the oscillograph trace. When the radiative heating rates were measured, the surface of the calorimeter was blackened with camphor soot to give an absorptivity of approximately unity. The run-to-run deviations from the nominal convective and radiative heating rates were ± 10 Btu/ft²-sec and ± 15 Btu/ft²-sec, respectively.

RESULTS AND DISCUSSION

The test results and other information for the 46 different materials tested during this investigation are presented in figures 6 through 53. The maximum back-surface temperature rises and weight losses of the materials are shown in figures 6 and 7, respectively. Individual data sheets summarizing the test results and the available physical characteristics of each material are presented in figures 8 through 53. (See table I for a list of the materials, the corresponding code numbers, the manufacturer or source of the material, and the figure number of the pertinent data sheet.) These data sheets include the composition of the material (where available), the average density, the percentage of the average weight lost during the test, the time history of the back-surface temperature, a photograph of the ablated surface, and a photograph comparing the profile of the model before and after the test. The profile pictures generally show the post-run silhouette in black and the original profile as a light half-tone area. In some cases the material expanded (as in fig. 24),

DECLASSIFIED

in which case the original profile is black and the after-run profile is indicated by the dark half-tone area. In figure 21, the black and light half-tone areas are the original profile and the black and dark half-tone areas indicate the after-run profile.

The results shown in figure 6 indicate the relative performance of the materials at the imposed test conditions. In most cases, at least two models of each material were tested. The crosshatching on the bar chart of figure 6 indicates the maximum spread in the back-surface temperatures measured for two or more samples of the same material. It is apparent that there are very large differences in the heat shielding ability of the various materials tested. The lowest back-surface temperature rises, obtained with balsa wood (no. 44) and cork (no. 45), were several orders of magnitude less than the highest back-surface temperature rise obtained with graphite (no. 41). Because of their low density, the initial weight of the test cores of balsa and cork was less than the standard core weight of the other materials. In order to compare the materials on an equal weight-per-unit-area basis, the back-surface temperature rises shown in figure 6 for these two materials have been adjusted for the differences in their initial core weights by the method shown in the appendix. Temperature rises computed by this method were in good agreement with measured temperatures for several cases where more than one core weight of the same material was tested.

The bar graph shown in figure 7 indicates the percent of the initial core weight lost by each ablation model during the test. The materials are arranged in the same order as in figure 6 (i.e., in order of increasing back-surface temperature rise starting at the top of the graphs). All of the weight-loss values shown, including those for balsa wood (no. 44) and cork (no. 45), are based on an initial test-core weight of 0.00250 pound. It is apparent that there is no correlation between the weight of material ablated and the maximum temperature rise measured at the back surface of the material. The weight of material lost varied from a minimum of less than 1 percent of the initial weight for boron nitride (no. 42) to a maximum of about 39 percent for black Teflon (no. 38).

The temperature time histories shown in the data sheets indicate that the back surfaces of most of the materials did not reach maximum temperatures until approximately a minute or two after the heat pulse had ended. However, for a few materials which had very high thermal conductivity, such as graphite (no. 41), or which were transparent to the radiation flux, such as Lexan (no. 14) or white Teflon (no. 37), the temperature at the back surface reached a maximum in only a few seconds.

A comparison of the photographs of the models after testing illustrates the variety of ablated surfaces. Because of the small size of the available samples of materials MX-2625 (no. 20) and MX-2630A (no. 21), the shroud or outer part of these models was made of Bakelite (no. 35) instead of the test material; therefore, only the part of the photograph representing the center core of the model is indicative of the char formed by these two materials. The difference in the scale factor between the nose radius of the test model and the radius of a full-scale heat shield should be considered when the roughness of the ablated

0371000000

surfaces is compared. For example, a surface irregularity that appears to be large when viewed on the test model may be insignificant when compared to the nose radius of a full-scale heat shield.

The superimposed before-and-after silhouettes shown in the data sheets give a linear measurement of the ablation or recession of the models. In considering these silhouettes, it should be noted that as a result of the exposure to the heat pulse, some of the materials expanded and show an increase rather than a decrease in size. These photographs are also useful in illustrating the degree to which the models retained their original hemispherical shape. Since the convective heat-transfer rate can be shown to be inversely proportional to the square root of the nose radius, the convective cold-wall heating rate during the latter part of the heat pulse for some models may have been different from the heating rate indicated by the calorimeter model. However, for the worst case (where the hemispherical nose erodes to a flat face during the heat pulse) it can be shown that the total heating rate (convective and radiative) at the stagnation point of the model would be decreased less than 15 percent.

CONCLUDING REMARKS

The present survey provides a preliminary evaluation of 46 heat-shield materials. The materials were exposed for 15 seconds to the maximum radiative (140 Btu/ft²-sec) and convective (230 Btu/ft²-sec) heating rates expected for a manned lunar vehicle and were evaluated on the basis of the maximum temperature rise measured at the back surface of a given weight per unit area (4.7 lb/ft²) of heat shield.

In general, the lowest back-surface temperature rises were obtained with materials that had low density and low thermal conductivity, and the highest back-surface temperature rises were obtained with materials that had high thermal conductivity or that were transparent to the radiative heat flux. There appeared to be no general correlation between the maximum back-surface temperature rise and the amount of material ablated. Balsa wood and cork provided the lowest back-surface temperature rises (approximately 19° F for both materials) at the imposed test conditions. The back-surface temperature rises of a group of materials, which included an insulating plaster, oak wood, and a number of plastic compositions, were 2 to 5 factors higher than those of balsa wood or cork. Those of the remaining materials ranged from 10 to 100 times higher than those of balsa wood or cork. This third group of materials consisted of approximately one-half of the total number of materials tested.

Although the maximum back-surface temperature rise gives a direct indication of a heat shield's ability to limit the flow of heat to the interior of a vehicle, and therefore is of primary importance in the evaluation of a heat shield, other factors, such as strength, ease of fabrication, and reaction to space environment, must also be considered before the final evaluation of a heat-shield material can be made. Consequently, the preliminary evaluation of the heat-shield materials given in this report is not intended to be an absolute rating of the materials nor is it necessarily applicable to conditions that differ

DECLASSIFIED

appreciably from those of the present tests. As an example, the results of the present survey indicate that although the lowest back-surface temperatures were obtained with balsa wood and cork, the strength of the char formed by these two materials appeared to be relatively poor compared to that of the other materials. Therefore, for shear stresses higher than those of the present tests, it is possible that the weak char formed by balsa and cork would be mechanically eroded at a rate that would adversely affect their back-surface temperatures and their evaluation relative to other materials.

Ames Research Center
National Aeronautics and Space Administration
Moffett Field, Calif., Nov. 1, 1962

0371220034

APPENDIX

TEMPERATURE ADJUSTMENT FOR NONSTANDARD CORE WEIGHTS

The maximum temperature rise measured at the back surface of a test core of nonstandard weight can be adjusted to the maximum temperature rise corresponding to a test core of standard weight if it is assumed that the same total amount of heat is stored in both the standard and nonstandard test cores after a given heat input. The expression relating the temperature rise of the core may be written as

$$Q = (m_s - \Delta m_s)c_p \Delta T_s = (m_n - \Delta m_n)c_p \Delta T_n$$

where Q is the heat stored in the core, m is the initial weight of the core, Δm is the weight loss due to ablation, c_p is the specific heat of the material, ΔT is the temperature rise, and the subscripts s and n refer to the standard and nonstandard core weights, respectively. Since the weight loss due to ablation should be the same regardless of initial core weight, the ratio of standard to nonstandard temperature rise may be expressed as

$$\frac{\Delta T_s}{\Delta T_n} = \frac{m_n - \Delta m_n}{m_s - \Delta m_n}$$

DECLASSIFIED

REFERENCES

1. Lundell, John H., Winovich, Warren, and Wakefield, Roy M.: Simulation of Convective and Radiative Entry Heating. Second National Symposium on Hypervelocity Techniques, Denver, Colorado, March 19 and 20, 1962.
2. Shepard, C. E., and Winovich, Warren: Electrical-Arc Jets for Producing Gas Streams With Negligible Contamination. A.S.M.E. Plasma Jet Symposium Paper 61-WA-247, Dec. 1961.
3. Compton, Dale L., Winovich, Warren, and Wakefield, Roy M.: Measurements of the Effective Heats of Ablation of Teflon and Polyethylene at Convective Heating Rates From 25 to 420 Btu/ft²-sec. NASA TN D-1332, 1962.
4. Adams, Mac C.: Recent Advances in Ablation. ARS Jour., vol. 29, no. 9, Sept. 1959, pp. 625-632.

TABLE I.- INDEX OF TEST MATERIALS

Code No.	Material	Source	Figure
1	MX-A	Chance-Vought Corp.	8
2	MX-B	↓	9
3	MX-C		10
4	MX-D		11
5	X3040	Avco Corp.	12
6	X3043	↓	13
7	X5026		14
8	X5035	↓	15
9	CD		16
10	123C	General Electric Co.	17
11	124A	↓	18
12	223C		19
13	523C	↓	20
14	Lexan		21
15	MX-4961	Fiberite Corp.	22
16	MX-4962	↓	23
17	MX-4963		24
18	MX-4964		25
19	MX-1344-67		26
20	MX-2625		27
21	MX-2630A		28
22	MX-2646		29
23	MX-3581		30
24	MX-4925		31
25	MX-5675		32
26	MX-5683		33
27	MX-5700		34
28	MX-7500		35
29	150-RPD	Raybestos Manhattan, Inc.	36
30	154-RPD	↓	37
31	155-RPD		38
32	LS-10091		39
33	91-LD	American Reinforced Plastics	40
34	Astrolite 1201P	H. I. Thompson Fiber Glass	41
35	Bakelite	Bakelite Co.	42
36	Fortiflex	Celanese Corp.	43
37	White Teflon	E. I. DuPont De Nemours	44
38	Black Teflon	E. I. DuPont De Nemours	45
39	High dens. phenolic-nylon	NASA, Langley Res. Center	46
40	Low dens. phenolic-nylon	NASA, Langley Res. Center	47
41	Graphite	---	48
42	Boron nitride	---	49
43	Oak wood	---	50
44	Balsa wood	---	51
45	Cork	---	52
46	Vonolite plaster	Vonolite Products Co.	53

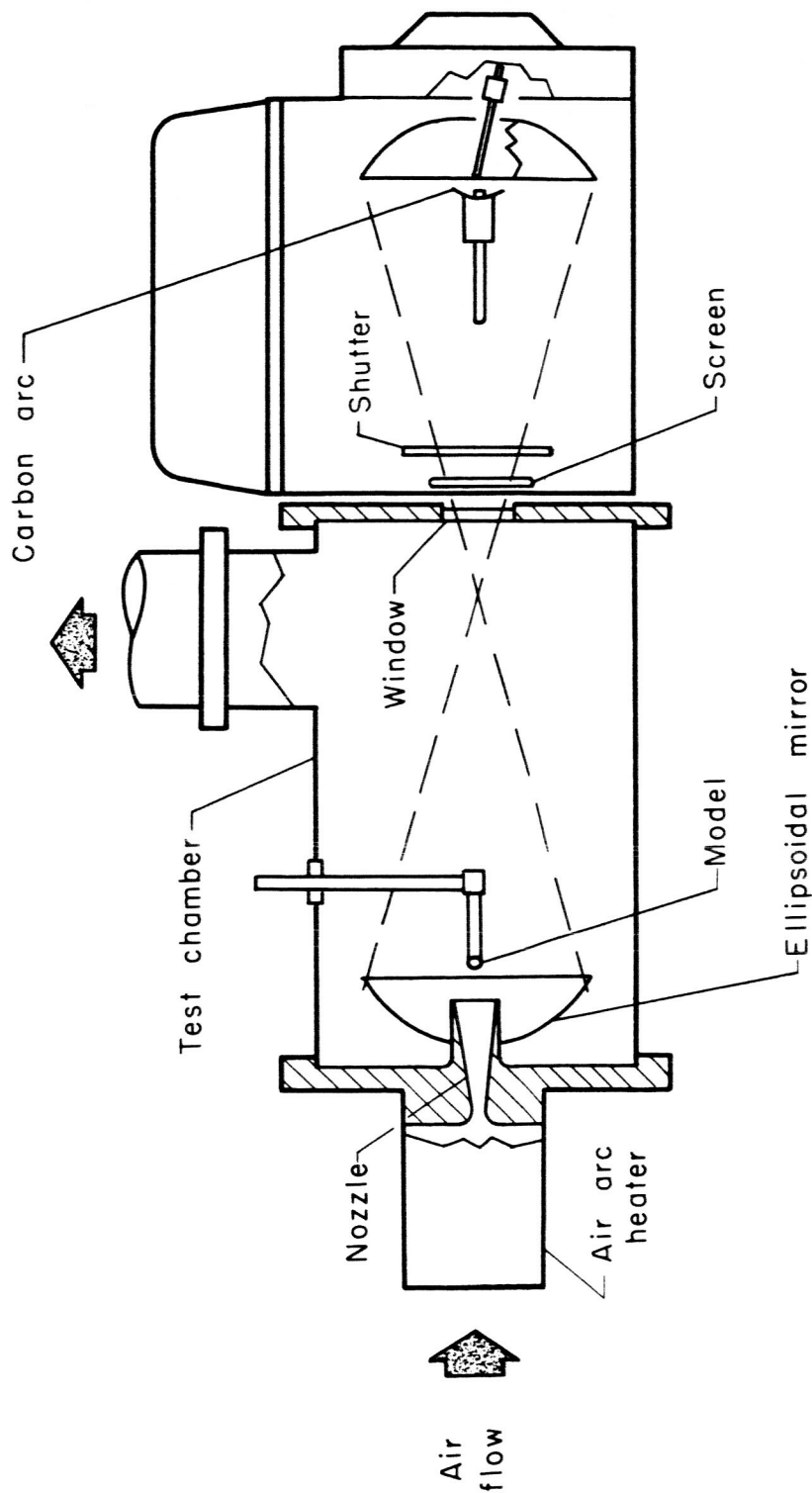
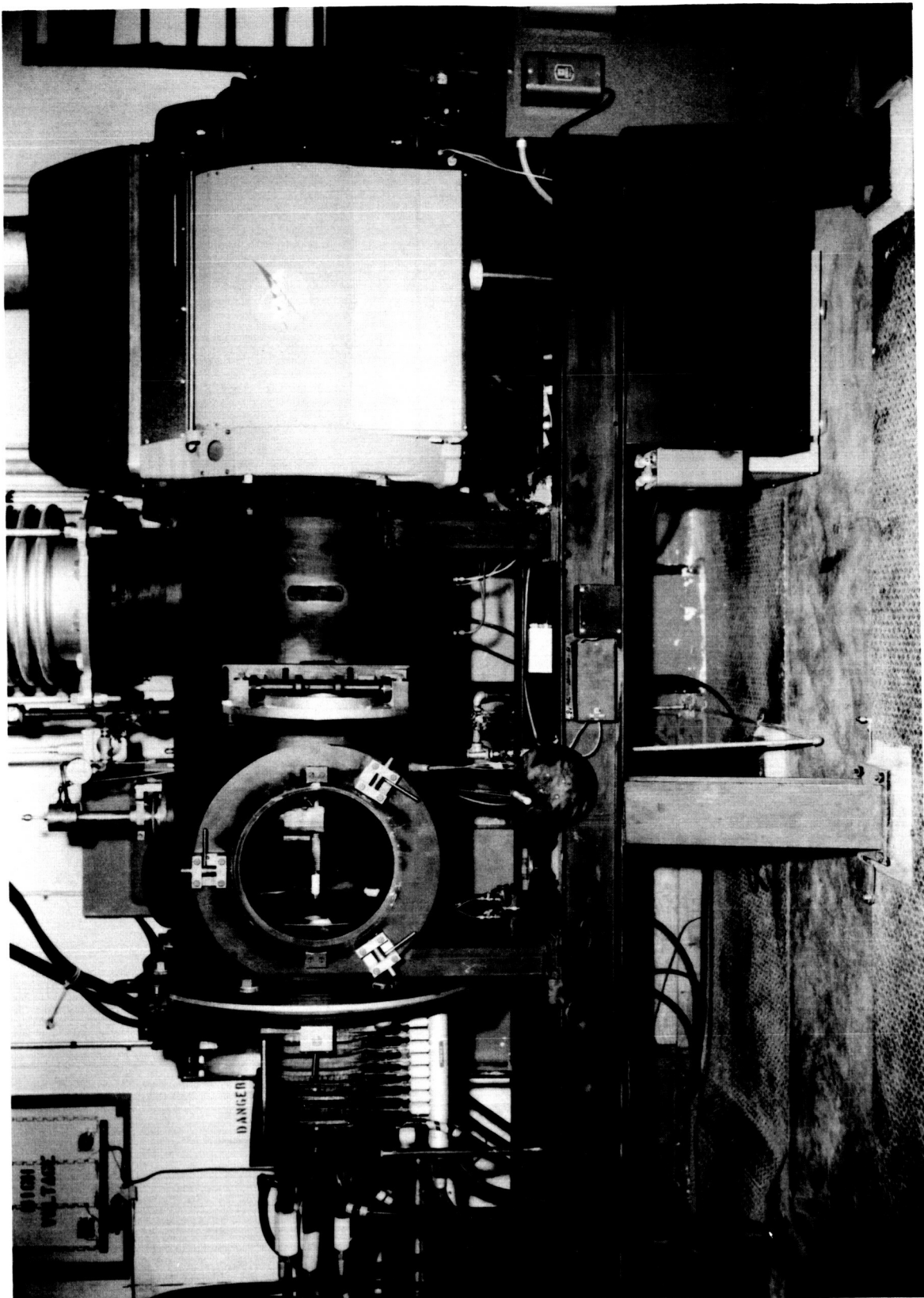


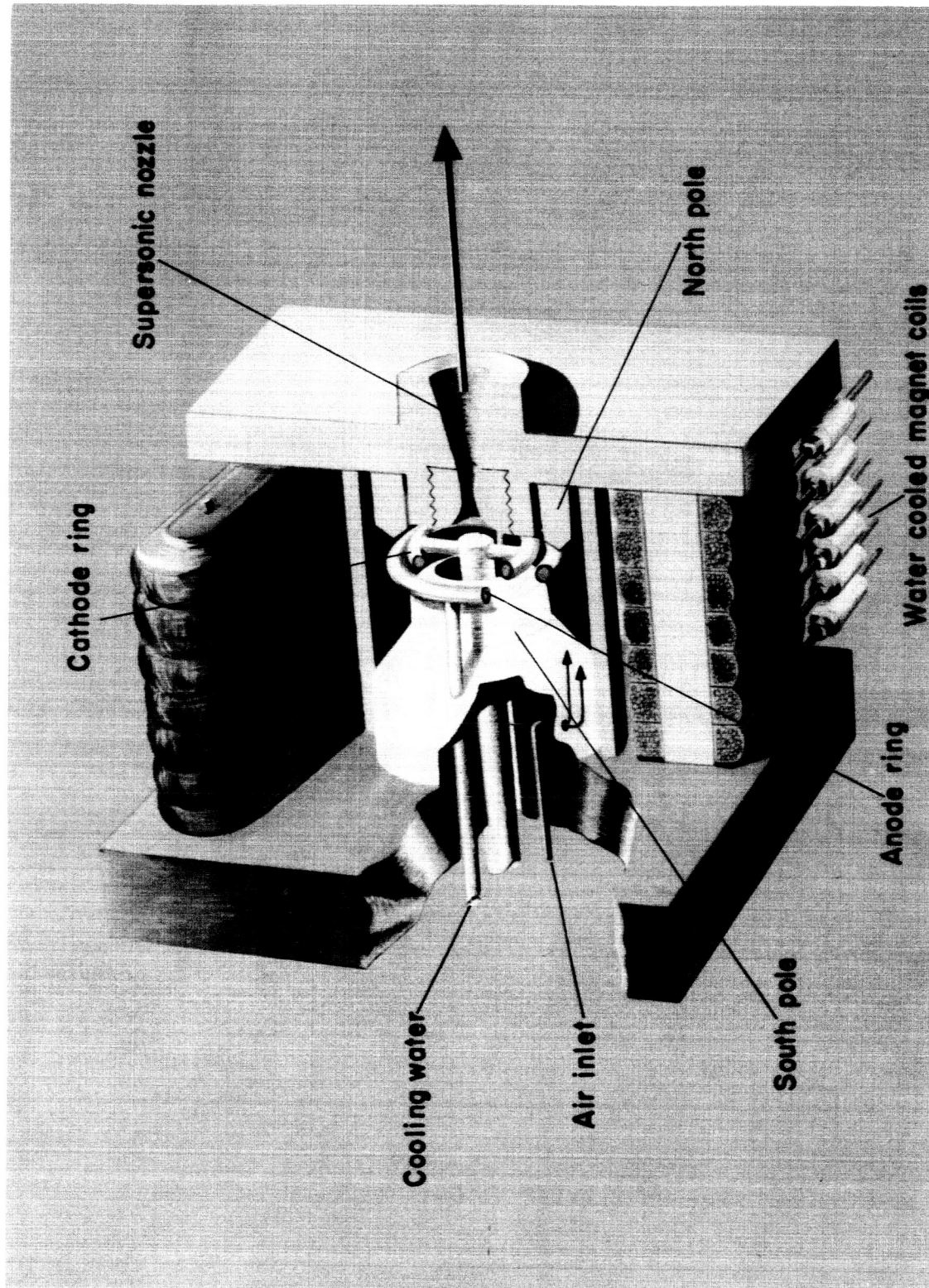
Figure 1.- Schematic diagram of the Ames entry heating simulator.

CONFIDENTIAL



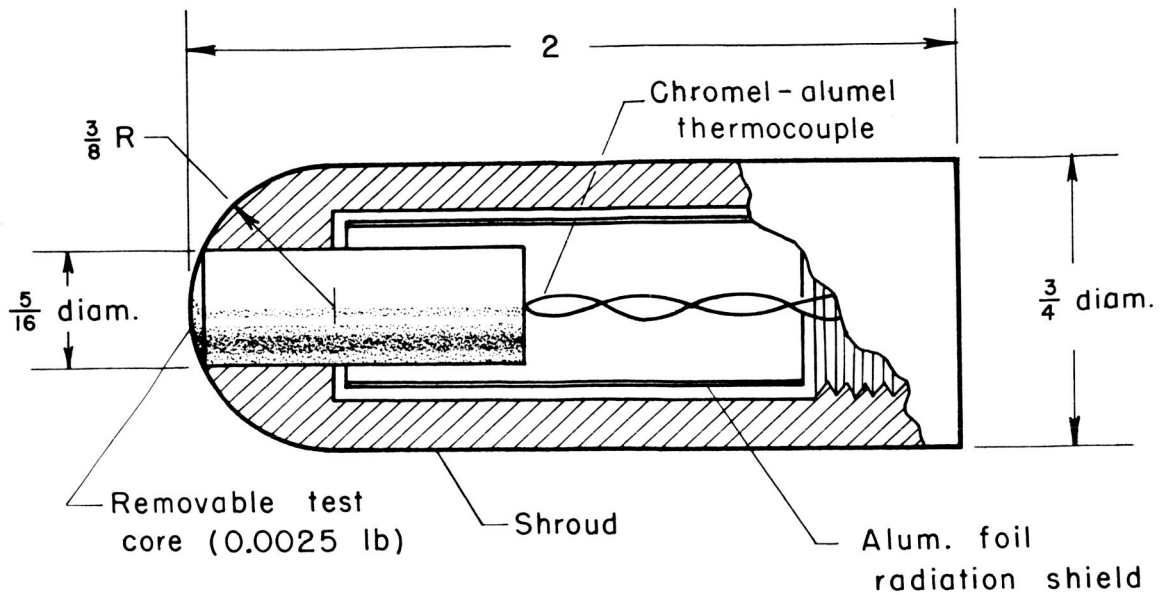
A-29985

Figure 2.- Photograph of the Ames entry heating simulator.



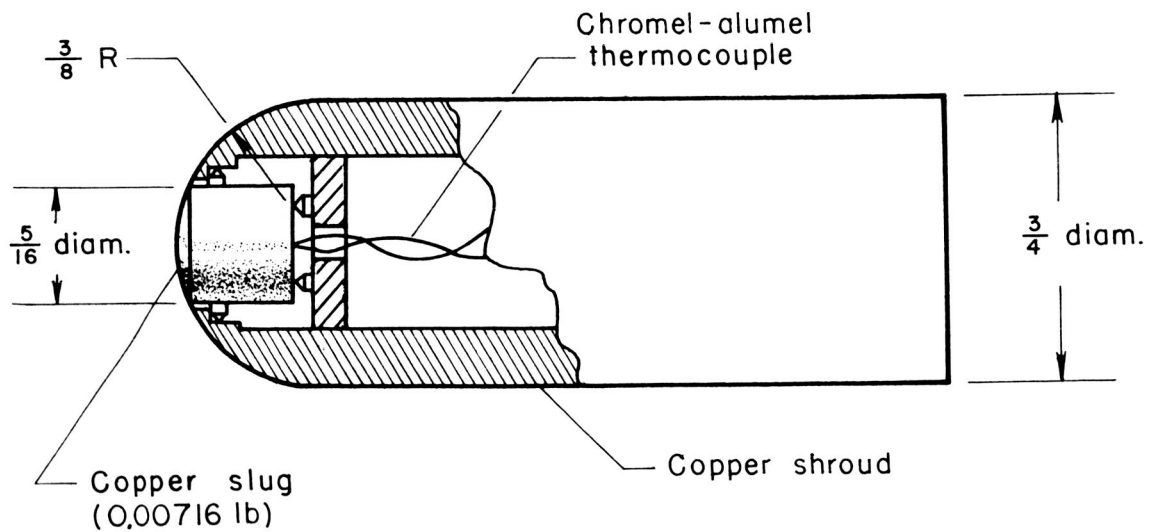
A-28321-16

Figure 3.- Arc-jet unit.



(a) Ablation model

All dimensions in inches
except as noted



(b) Calorimeter model

Figure 4.- Models.

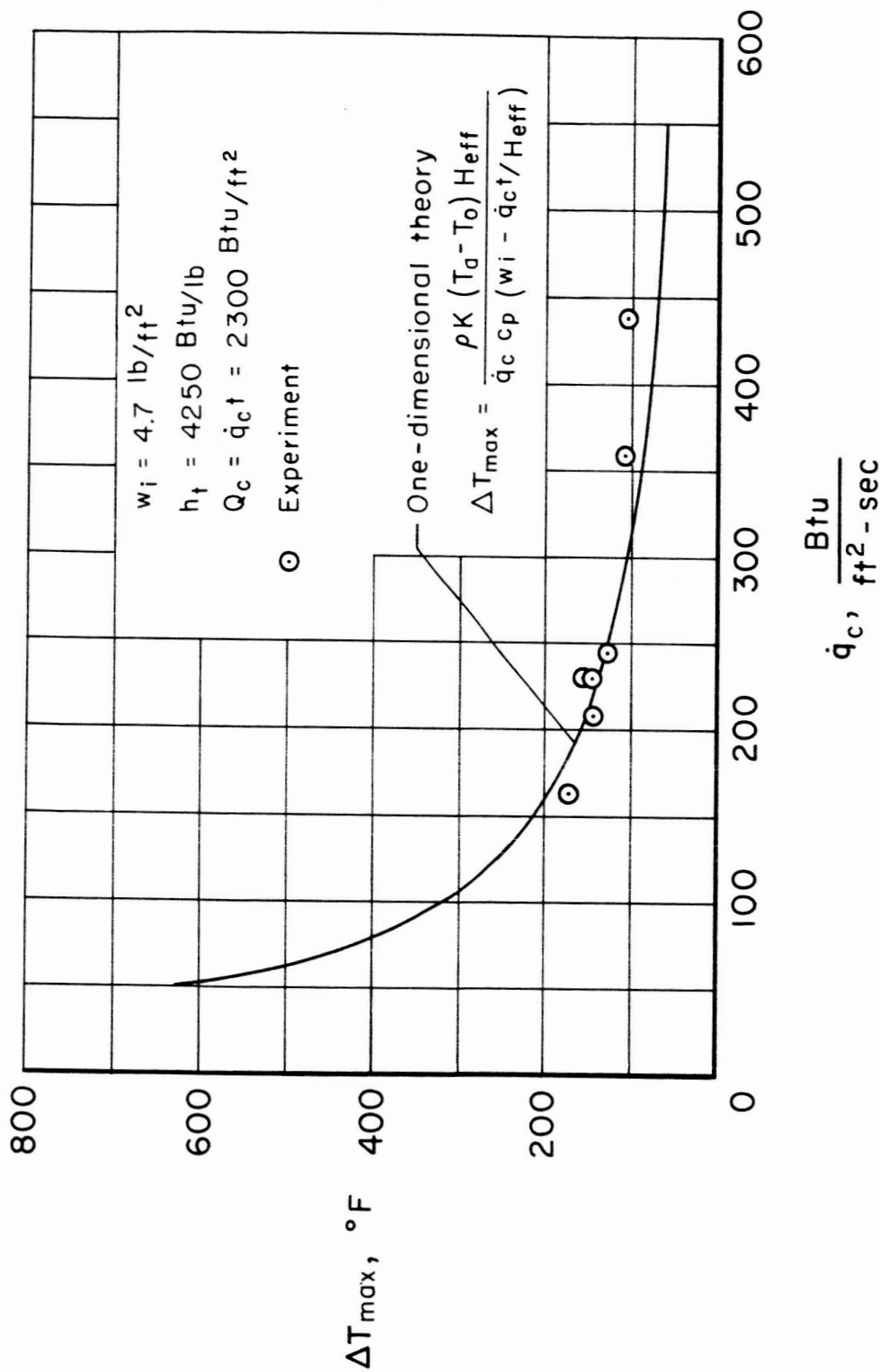


Figure 5.- Back-surface temperature rise of Teflon at various convective heating rates.

03 15 10 30

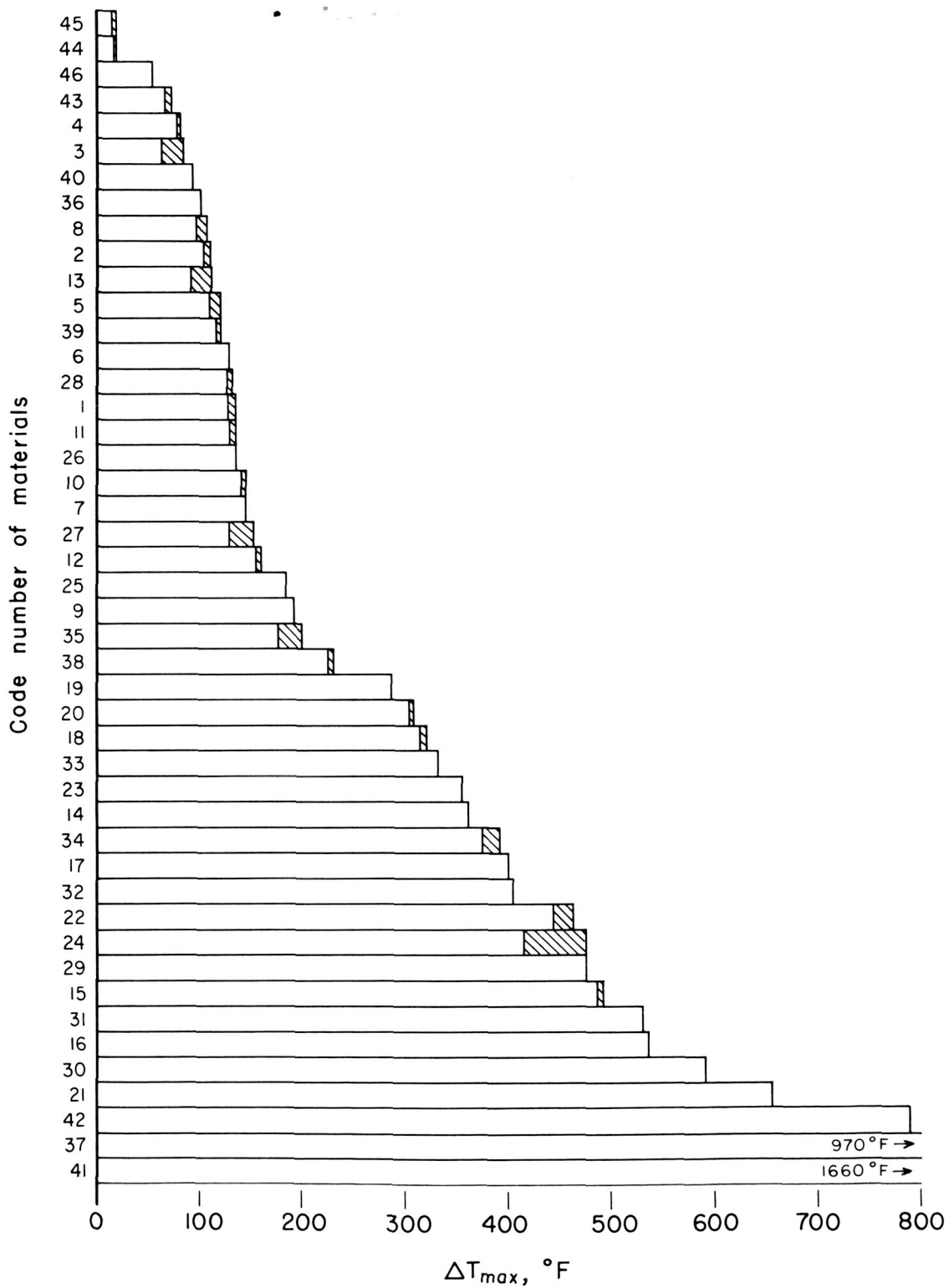


Figure 6.- Comparison of the maximum back-surface temperatures for equal weight per unit area of heat-shield material.

DECLASSIFIED

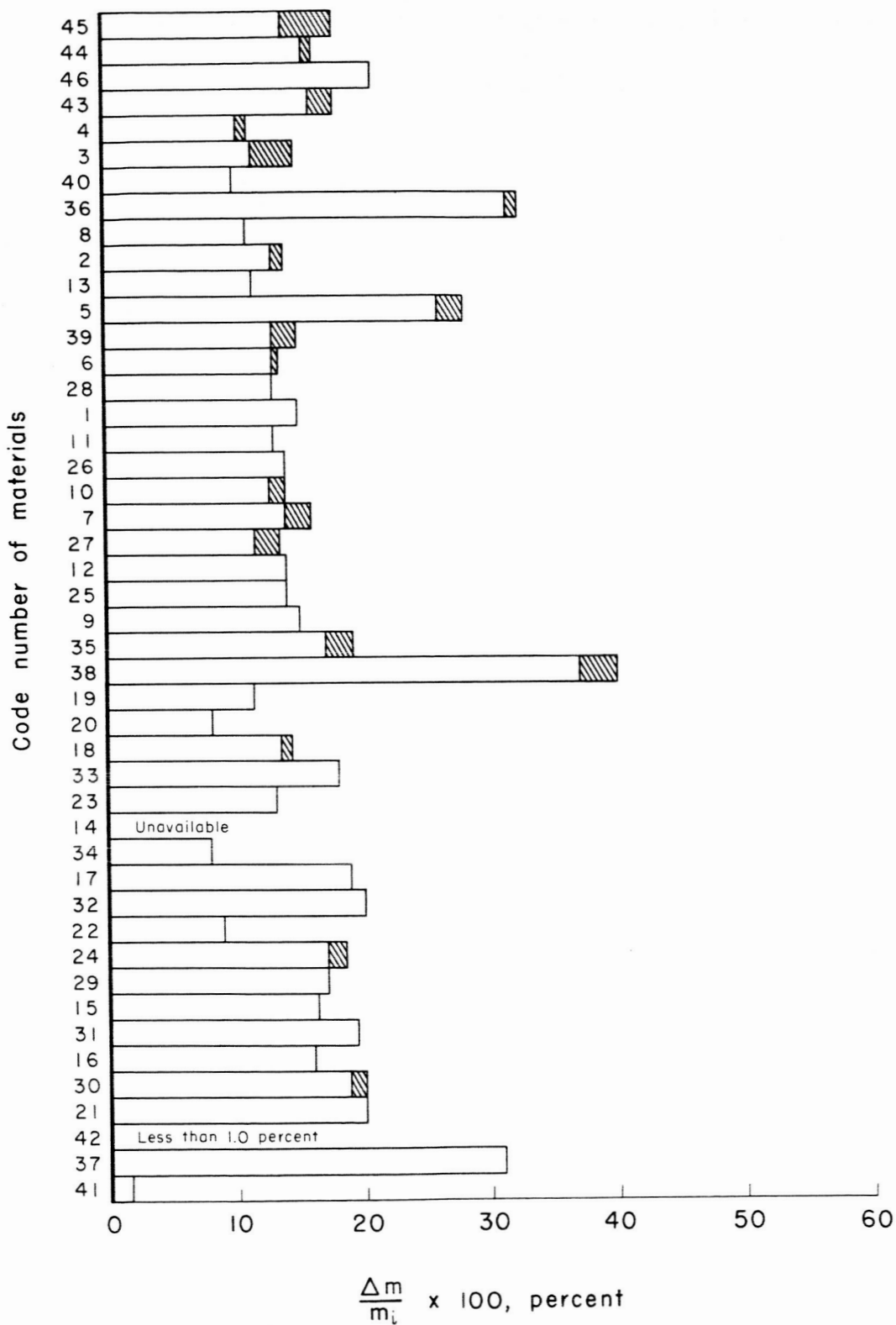


Figure 7.- Comparison of ablative weight loss of various materials.

037429.1030

Composition
(Unavailable)

Density = 81 lb/ft³

Wt. Loss = 15 %

$\Delta T_{\max} = 127 \text{ to } 135 \text{ }^{\circ}\text{F}$

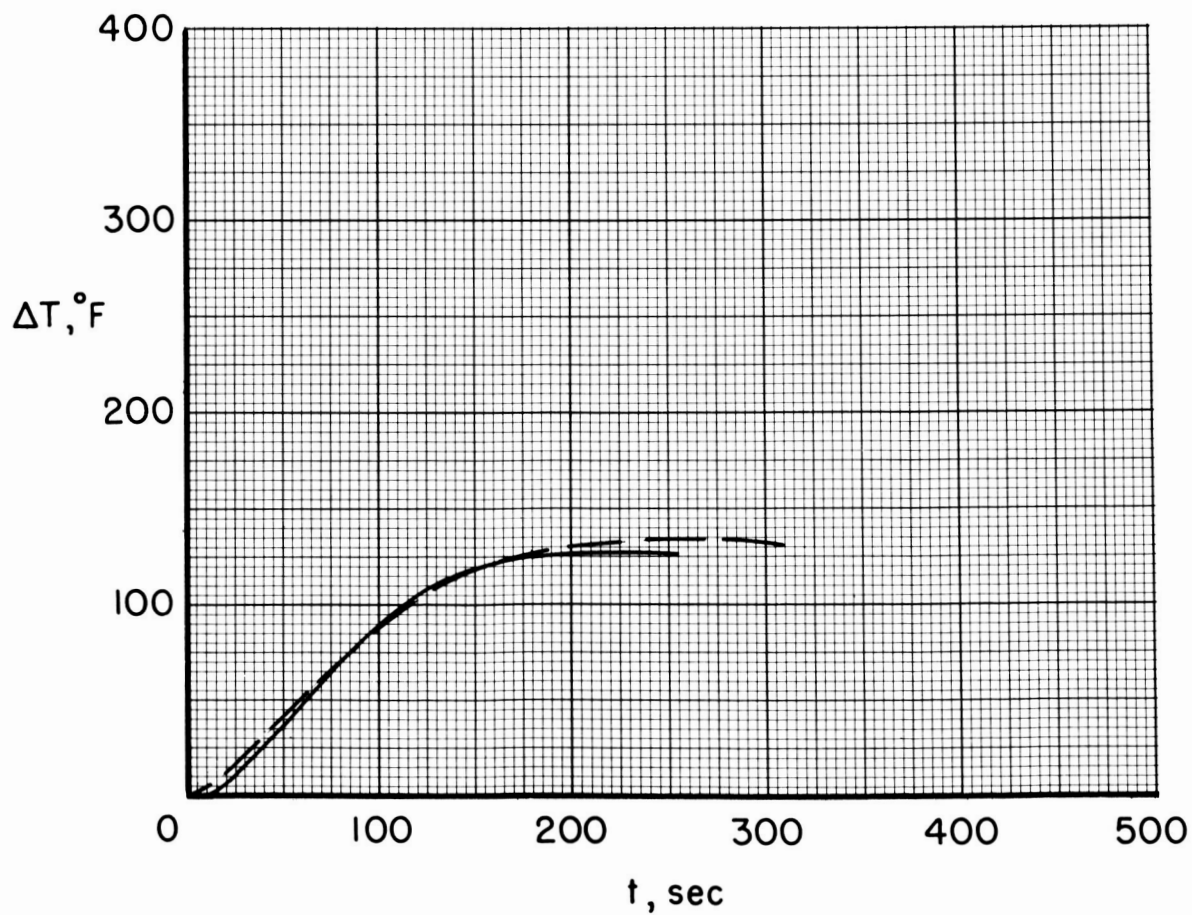


Figure 8.- Material number 1 (Chance-Vought MX-A).

DECLASSIFIED

Composition
(Unavailable)

Density = 60 lb/ft³

Wt. Loss = 14 %

$\Delta T_{\max} = 103 \text{ to } 109^\circ\text{F}$

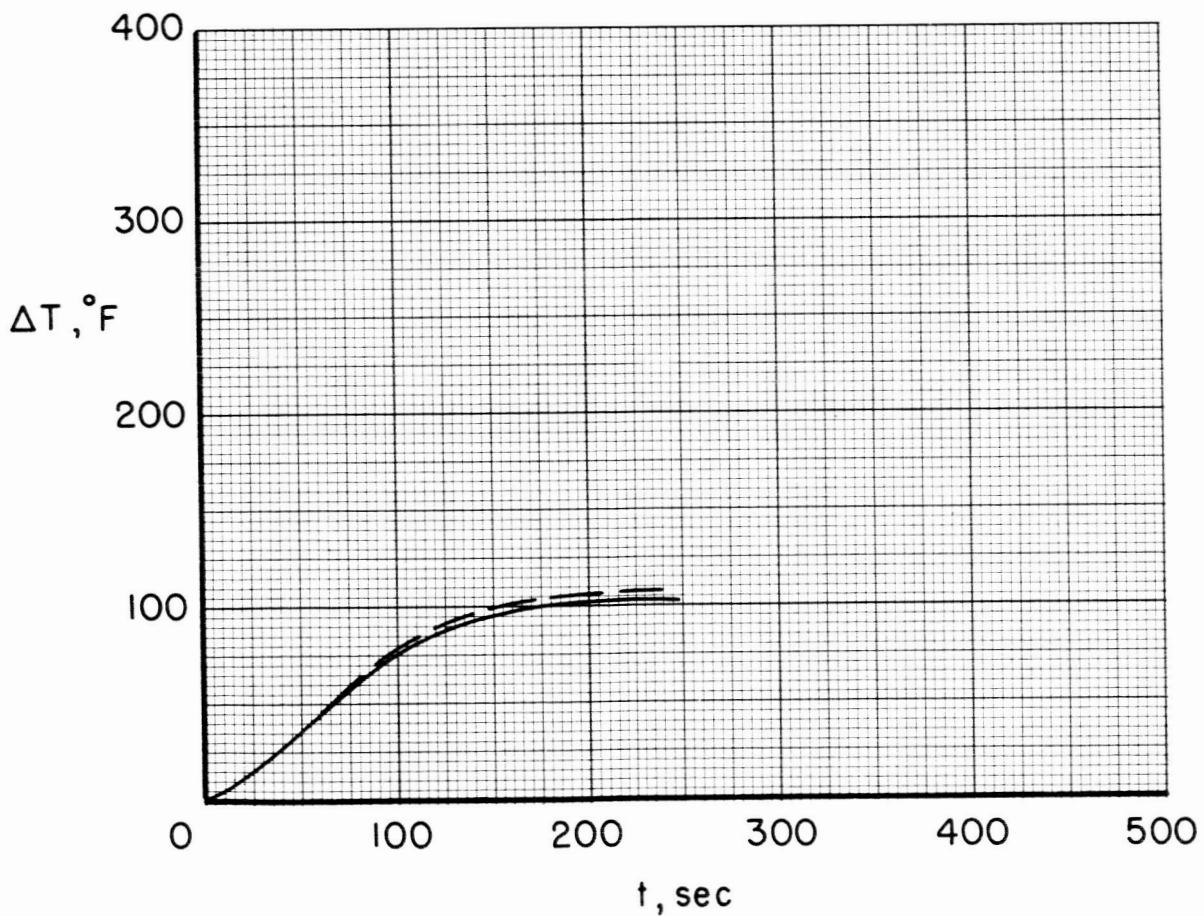


Figure 9.- Material number 2 (Chance-Vought MX-B).

03722030

Composition
(Unavailable)

Density = 37 lb/ft³

Wt. Loss = 13 %

ΔT_{\max} = 62 to 83 °F

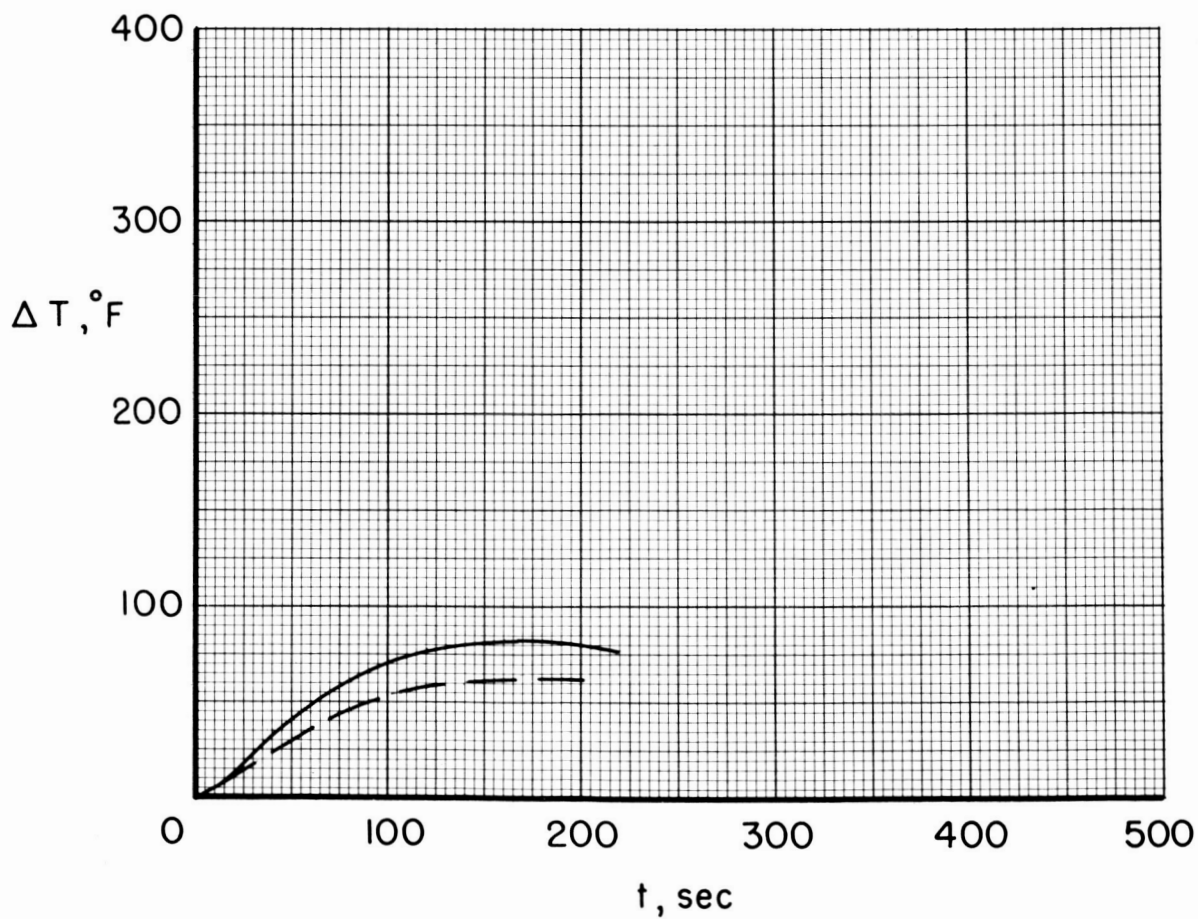


Figure 10.- Material number 3 (Chance-Vought MX-C).

DECLASSIFIED

Composition
(Unavailable)

Density = 39 lb/ft³

Wt. Loss = 11 %

$\Delta T_{\max} = 78 \text{ to } 81 \text{ }^{\circ}\text{F}$

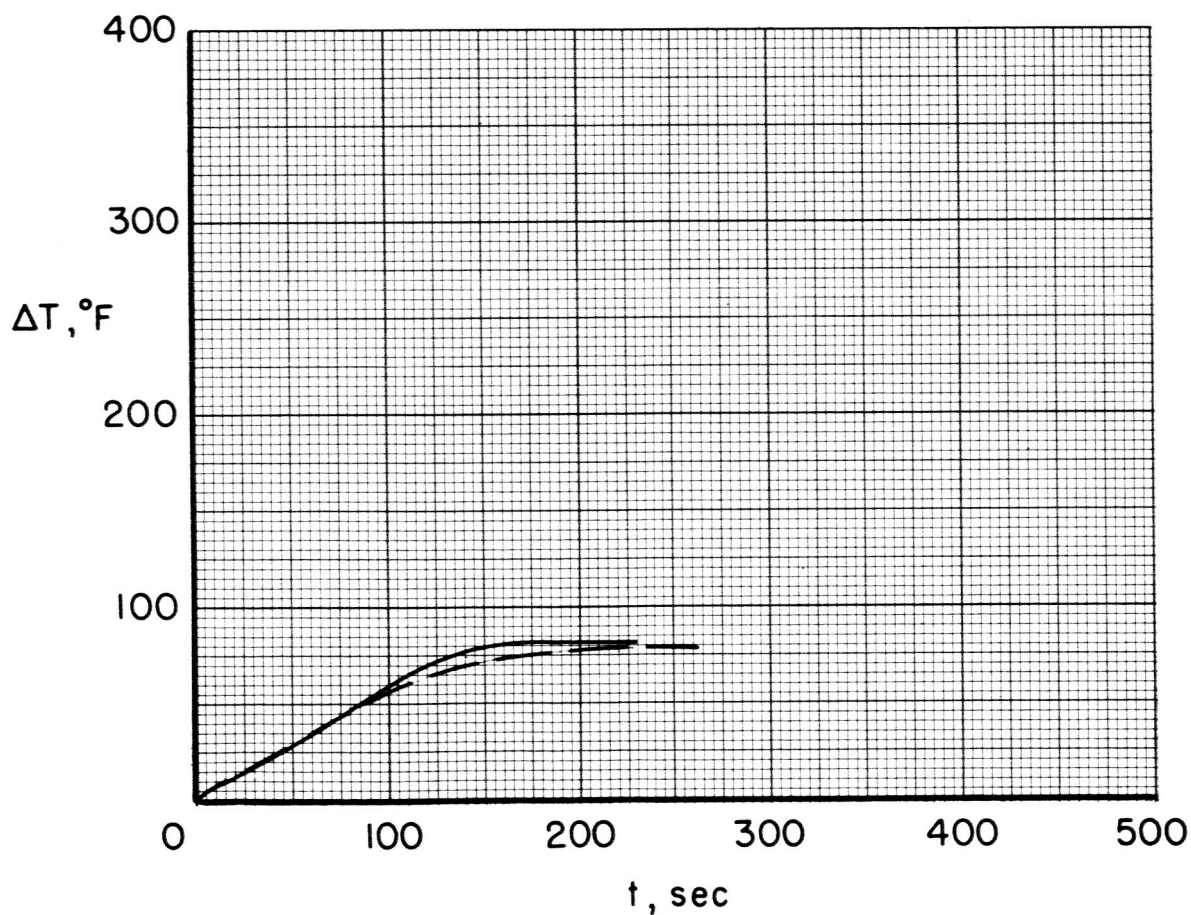


Figure 11.- Material number 4 (Chance-Vought MX-D).

0371291030

Composition
(Unavailable)

Density = 71 lb/ft³

Wt. Loss = 27 %

$\Delta T_{\max} = 108 \text{ to } 118 \text{ }^{\circ}\text{F}$

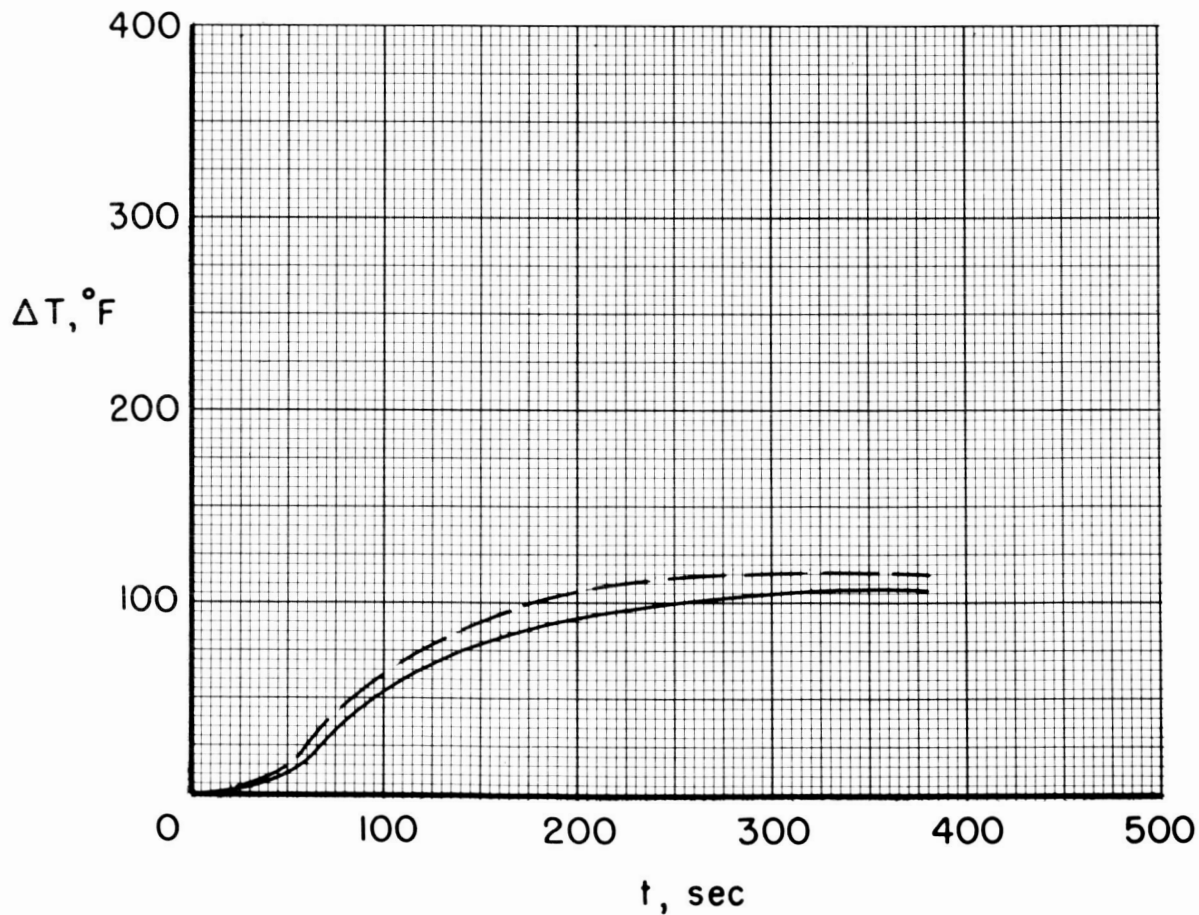


Figure 12.- Material number 5 (Avco X3040).

DECLASSIFIED

Composition
(Unavailable)

Density = 72 lb/ft³

Wt. Loss = 13 %

$\Delta T_{\max} = 128^{\circ}\text{F}$

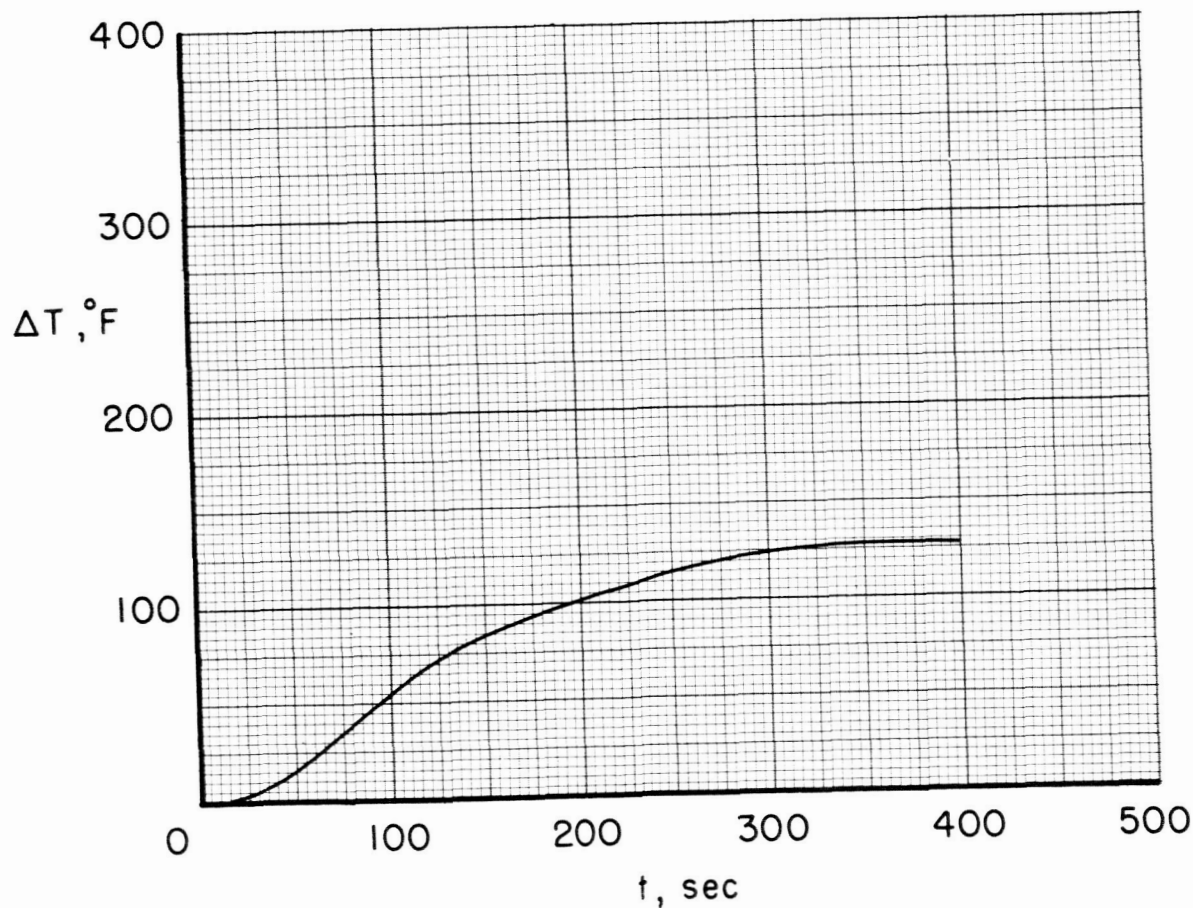


Figure 13.- Material number 6 (Avco X3043).

031715-1030

Composition
(Unavailable)

Density = 78 lb/ft³

Wt. Loss = 15 %

$\Delta T_{\max} = 145^{\circ}\text{F}$

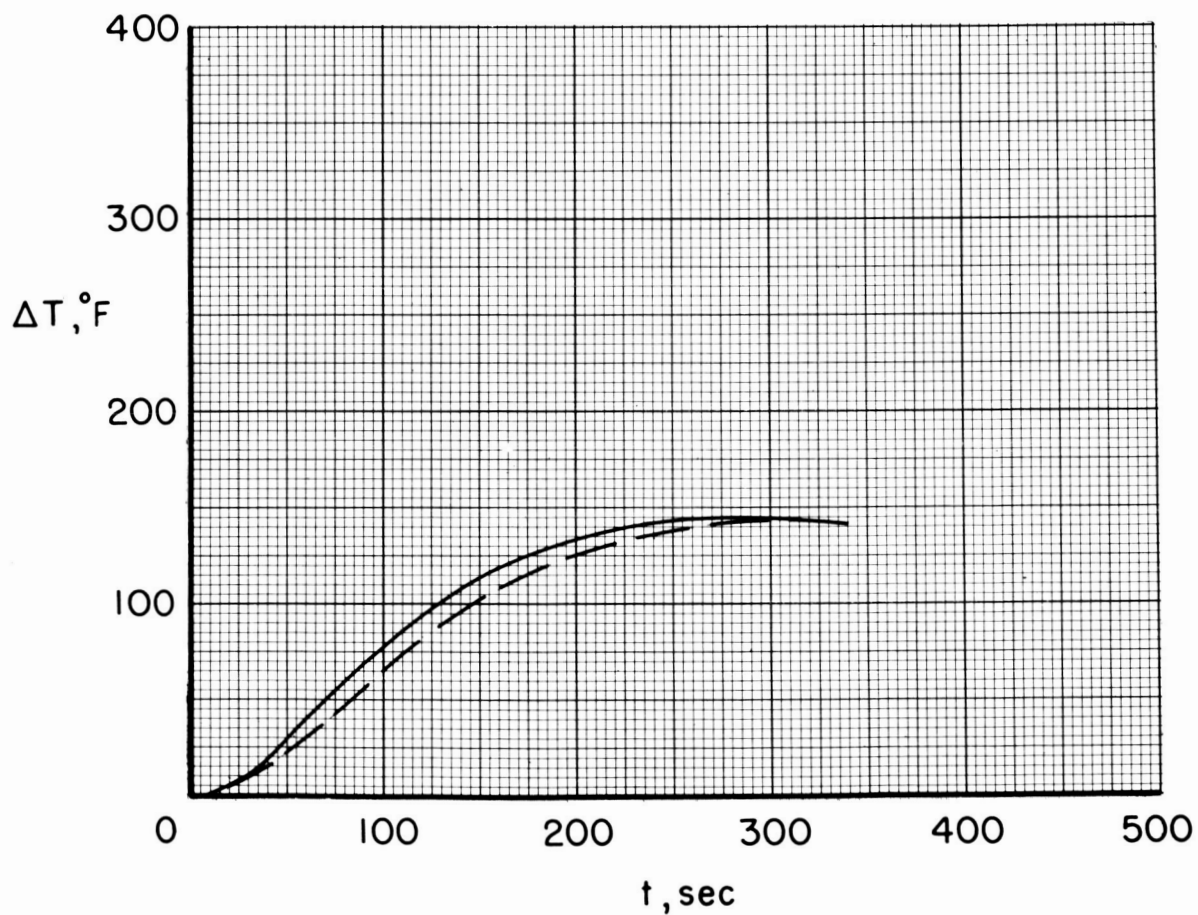


Figure 14.- Material number 7 (Avco X5026).



Composition
(Unavailable)

Density = 44 lb/ft³

Wt. Loss = 11 %

$\Delta T_{\max} = 96 \text{ to } 106 \text{ }^{\circ}\text{F}$

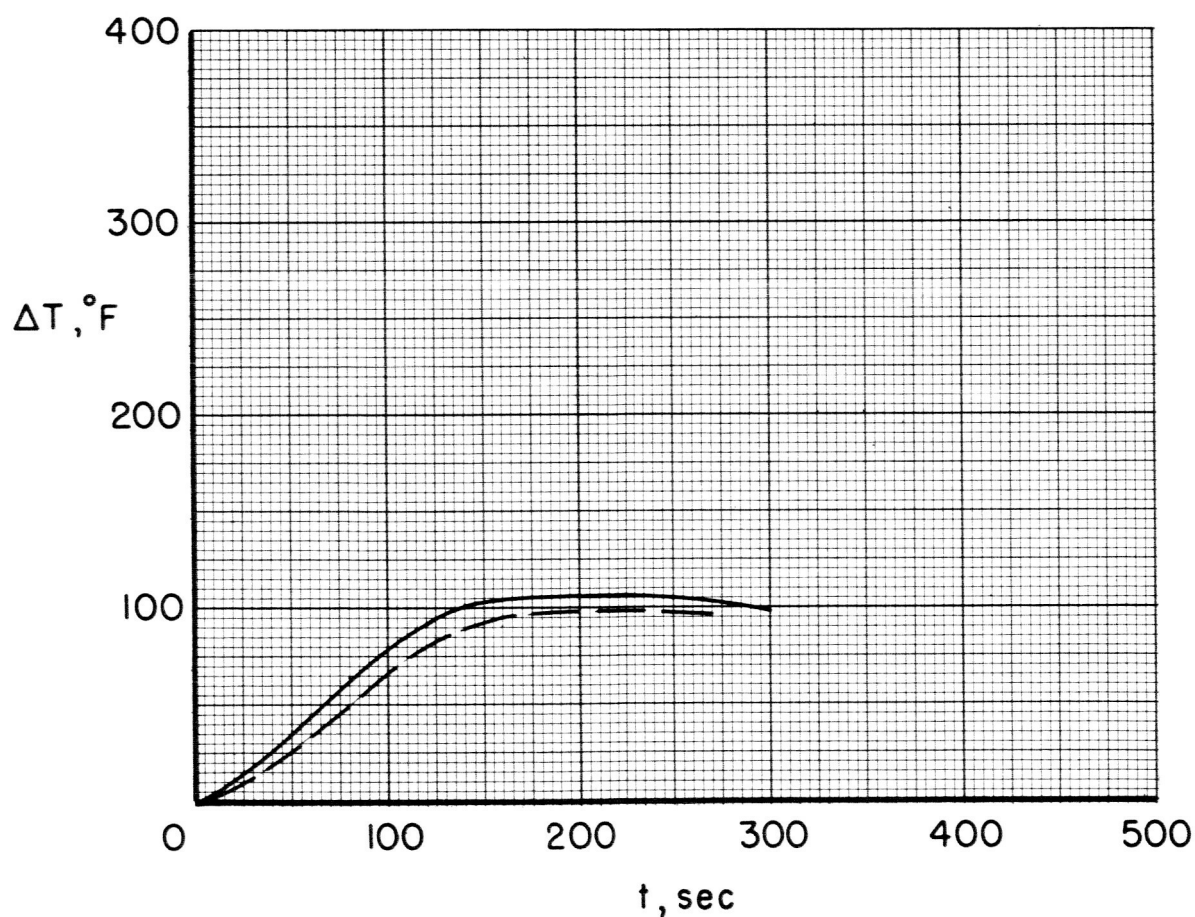


Figure 15.- Material number 8 (Avco X5035).





Composition
(Unavailable)

Density = 86 lb/ft³

Wt. Loss = 15 %

$\Delta T_{\max} = 192^{\circ}\text{F}$

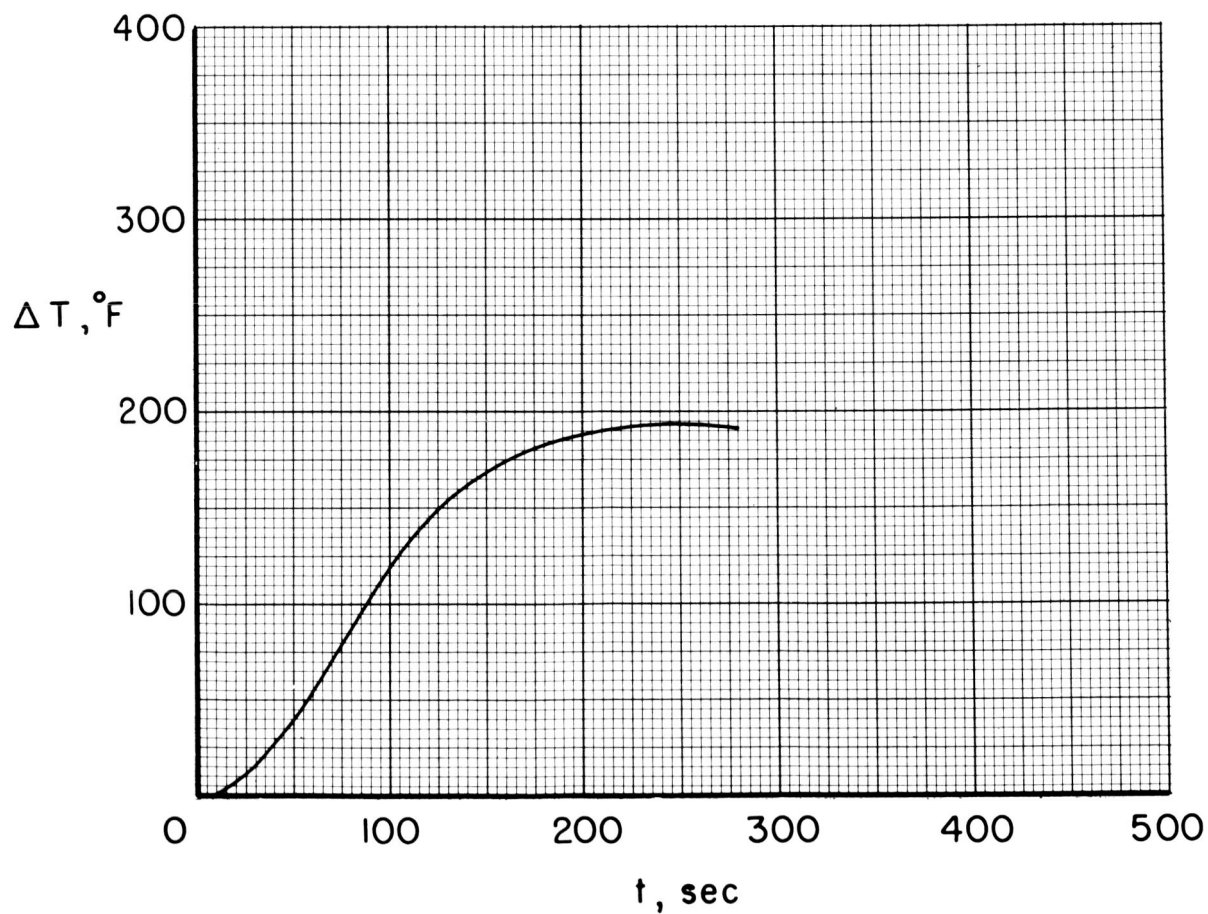
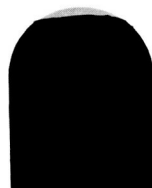
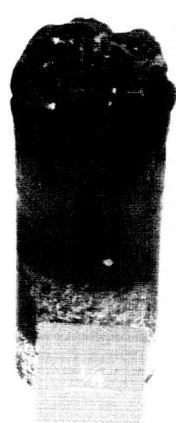
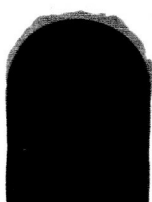


Figure 16.- Material number 9 (Avco CD).



NO. 1037A



Composition

(Unavailable)

Density = 76 lb/ft³

Wt. Loss = 13 %

$\Delta T_{\max} = 142 \text{ to } 144^{\circ}\text{F}$

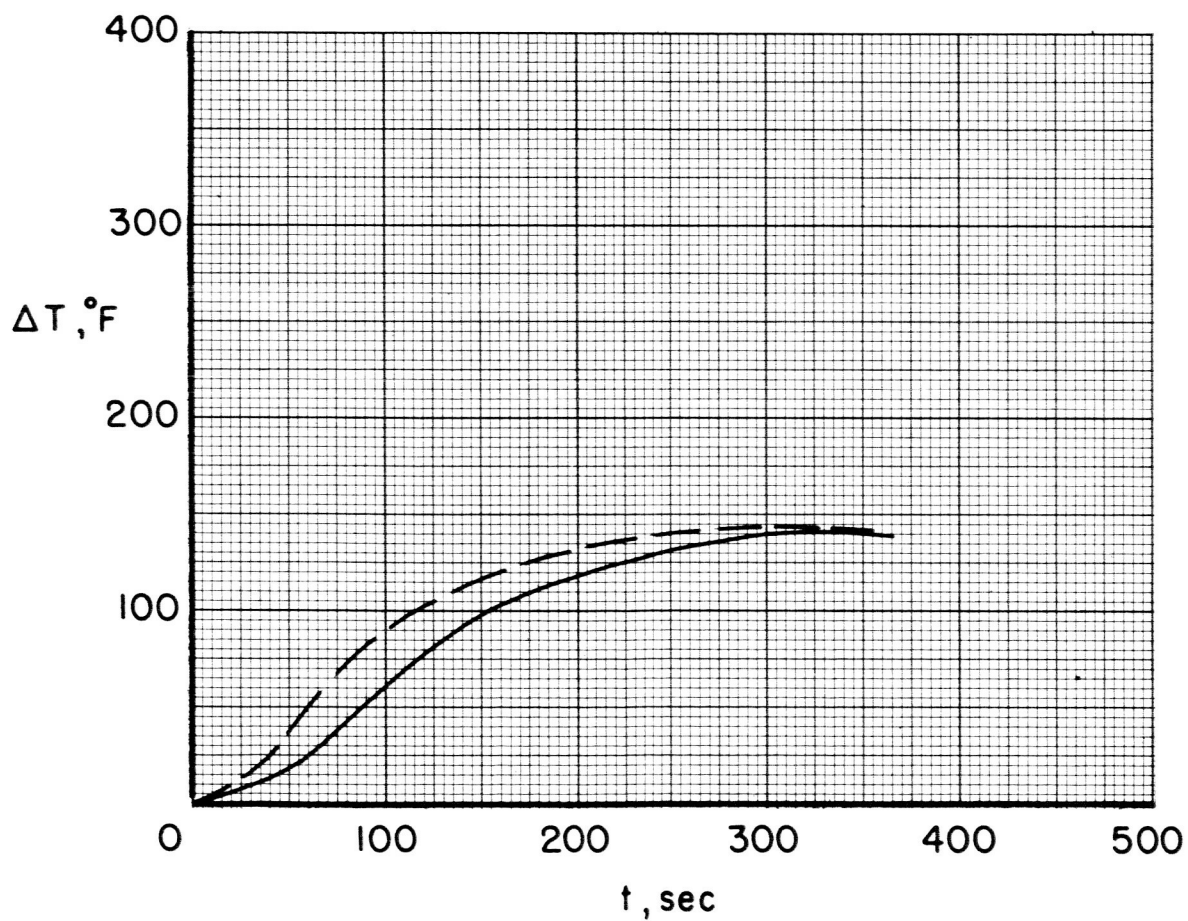


Figure 17.- Material number 10 (G.E. 123C).





Composition
(Unavailable)

Density = 76 lb/ft³

Wt. Loss = 13 %

$\Delta T_{\max} = 129 \text{ to } 134^{\circ}\text{F}$

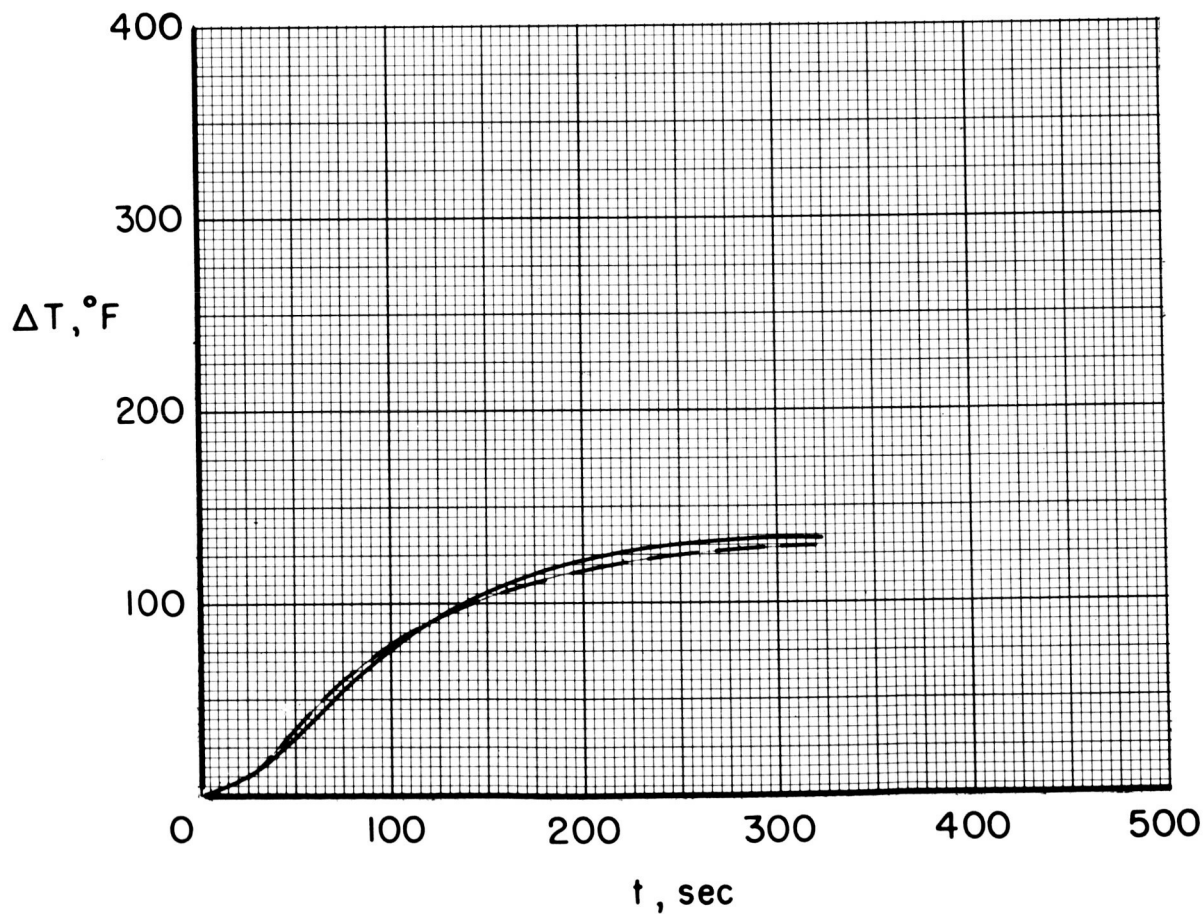


Figure 18.- Material number 11 (G.E. 124A).





Composition
(Unavailable)

Density = 80 lb/ft³

Wt. Loss = 14 %

$\Delta T_{\max} = 155 \text{ to } 159^\circ\text{F}$

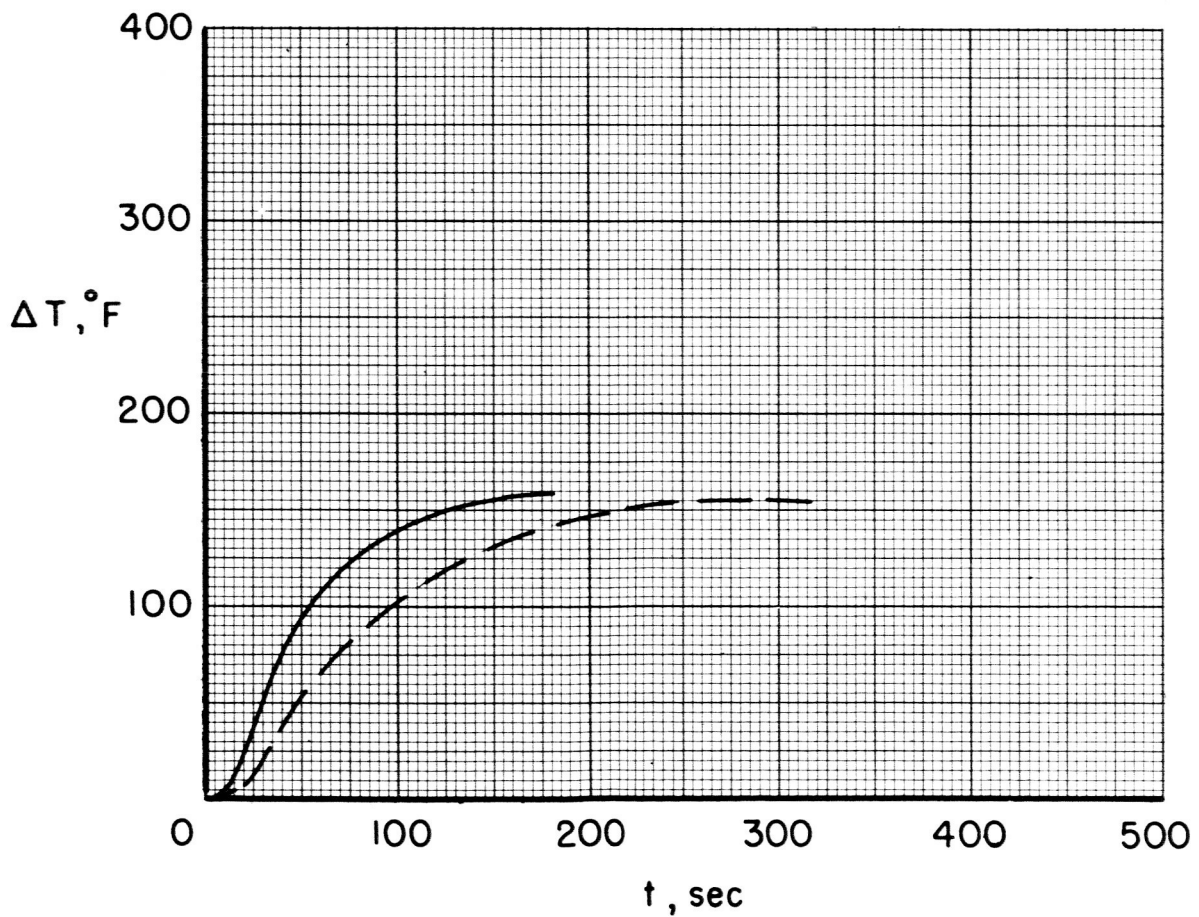
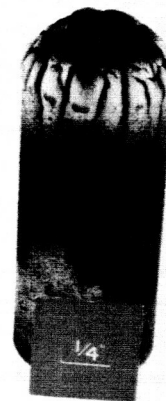
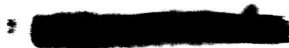


Figure 19.- Material number 12 (G.E. 223C).



SECRET



Composition
(Unavailable)

Density = 48 lb/ft³

Wt. Loss = 11 %

$\Delta T_{\max} = 91 \text{ to } 111 \text{ } ^\circ\text{F}$

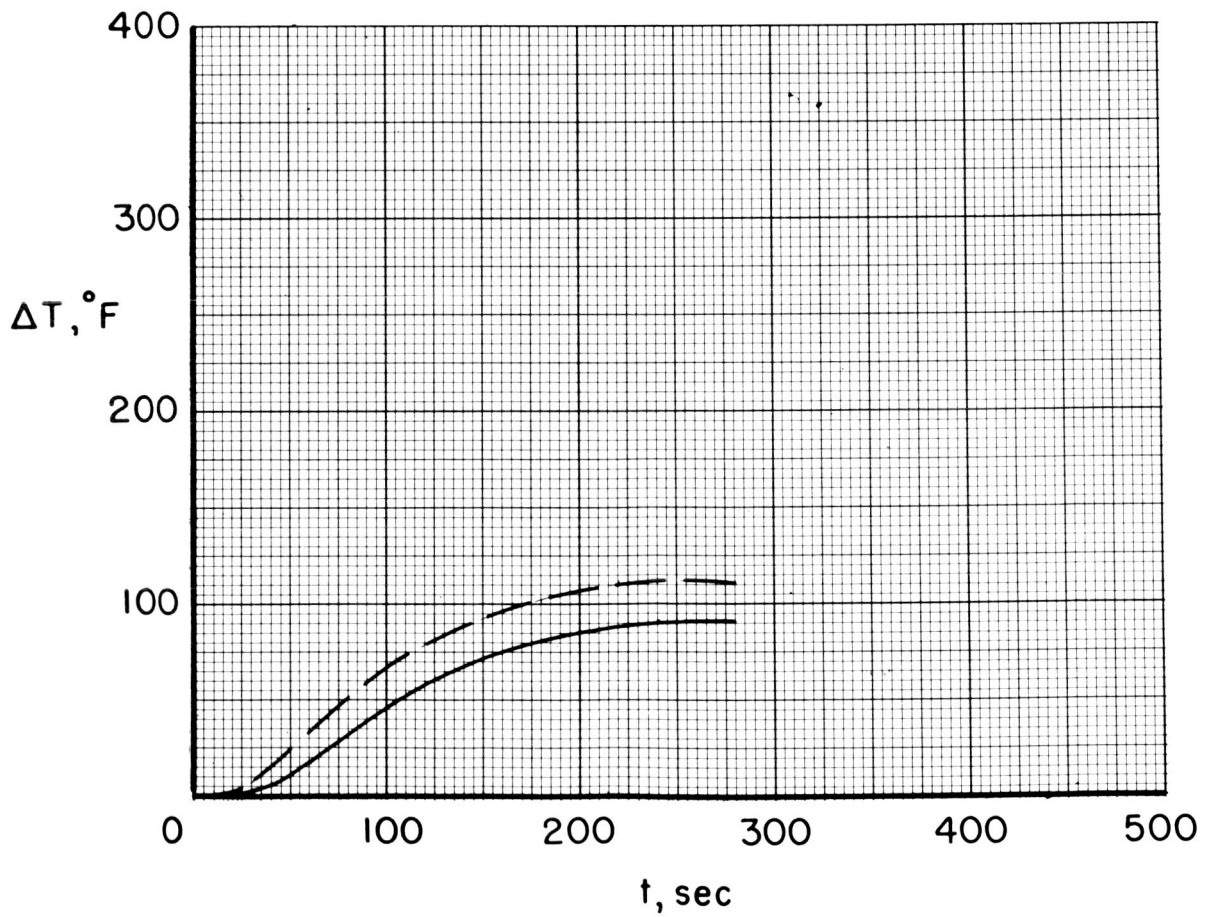


Figure 20.- Material number 13 (G.E. 523C).

SECRET

DECLASSIFIED

Composition
(Unavailable)

Density = 75 lb/ft³

Wt. Loss = (unavailable)

$\Delta T_{\max} = 362^{\circ}\text{F}$

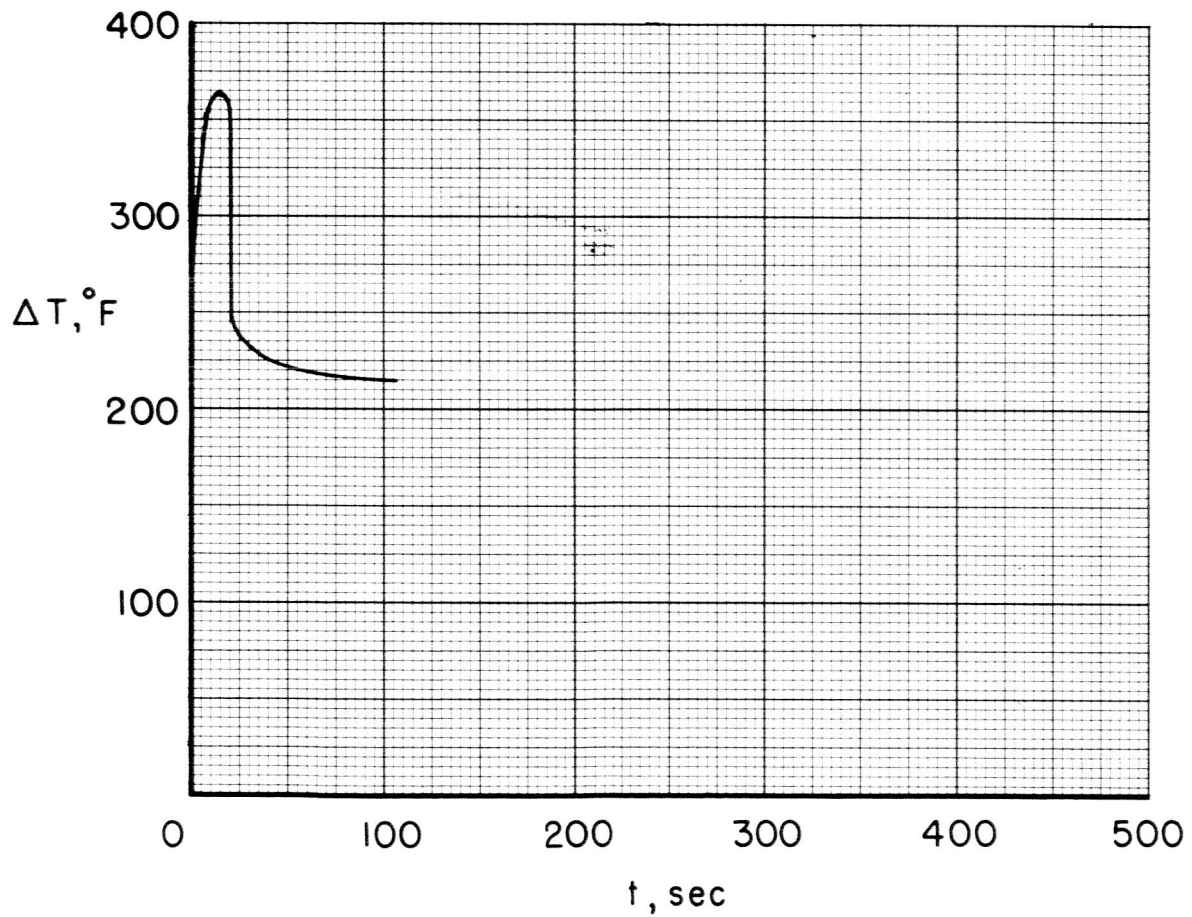
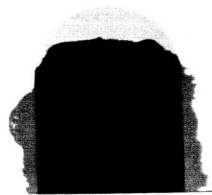
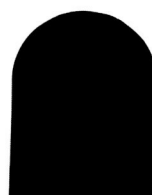
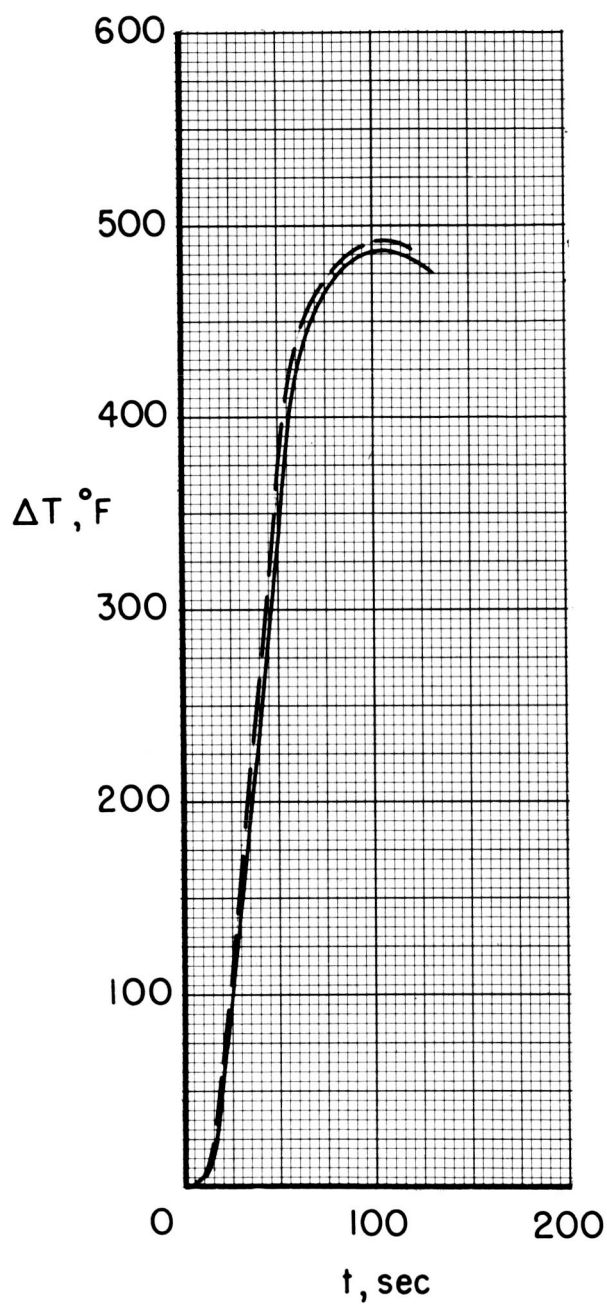


Figure 21.- Material number 14 (G.E. Lexan).





Composition

Phenolic resin

Polyamide

Graphite cloth

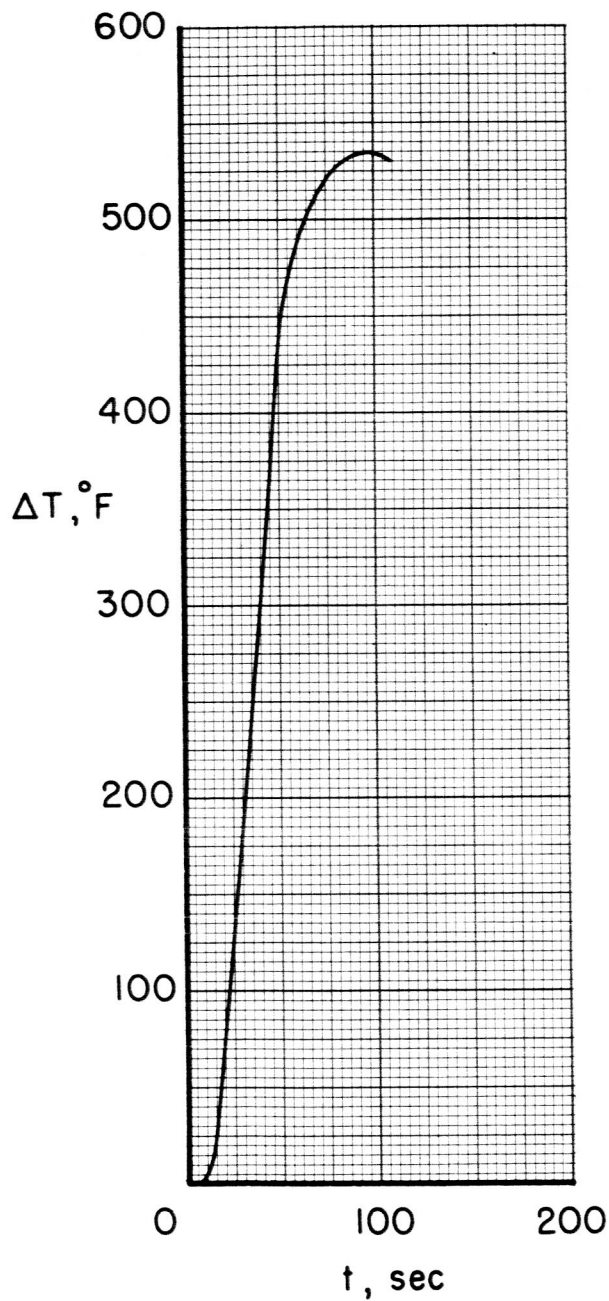
Density = 85 lb/ft³

Wt. Loss = 16 %

$\Delta T_{\max} = 488 \text{ to } 493 \text{ }^{\circ}\text{F}$

Figure 22.- Material number 15 (Fiberite MX-4961).

DECLASSIFIED



Composition

Phenolic resin

Polyamide

Graphite cloth

Density = 87 lb/ft³

Wt. Loss = 16 %

$\Delta T_{\max} = 536 ^\circ F$

Figure 23.- Material number 16 (Fiberite MX-4962).

DECLASSIFIED

Composition

Phenolic resin

Graphite cloth

Density = 87 lb/ft³

Wt. Loss = 14 %

$\Delta T_{\max} = 316 \text{ to } 321 ^\circ\text{F}$

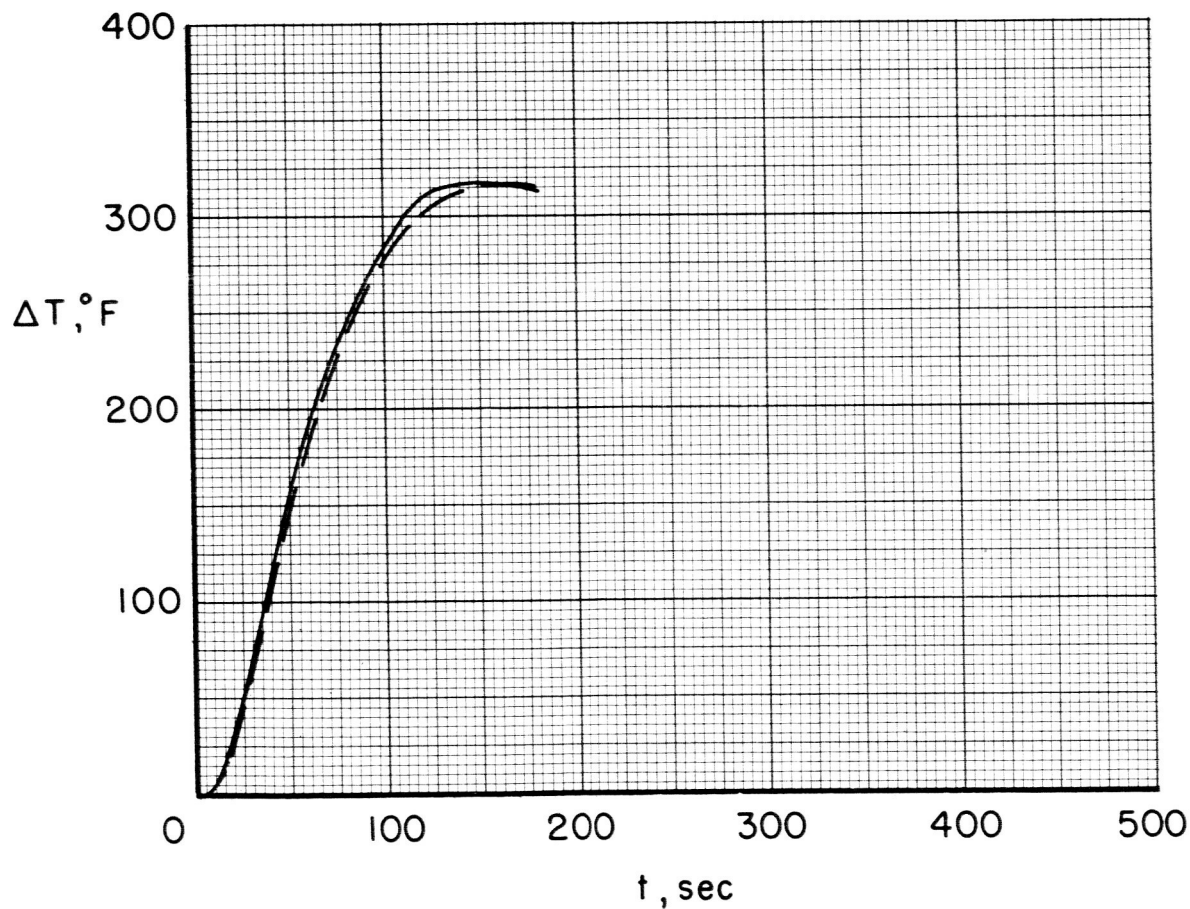


Figure 25.- Material number 18 (Fiberite MX-4964).



037154030

Composition

Phenolic resin

Quartz fibers

Mineral filler

Density = 109 lb/ft³

Wt. Loss = 11 %

$\Delta T_{\max} = 287^{\circ}\text{F}$

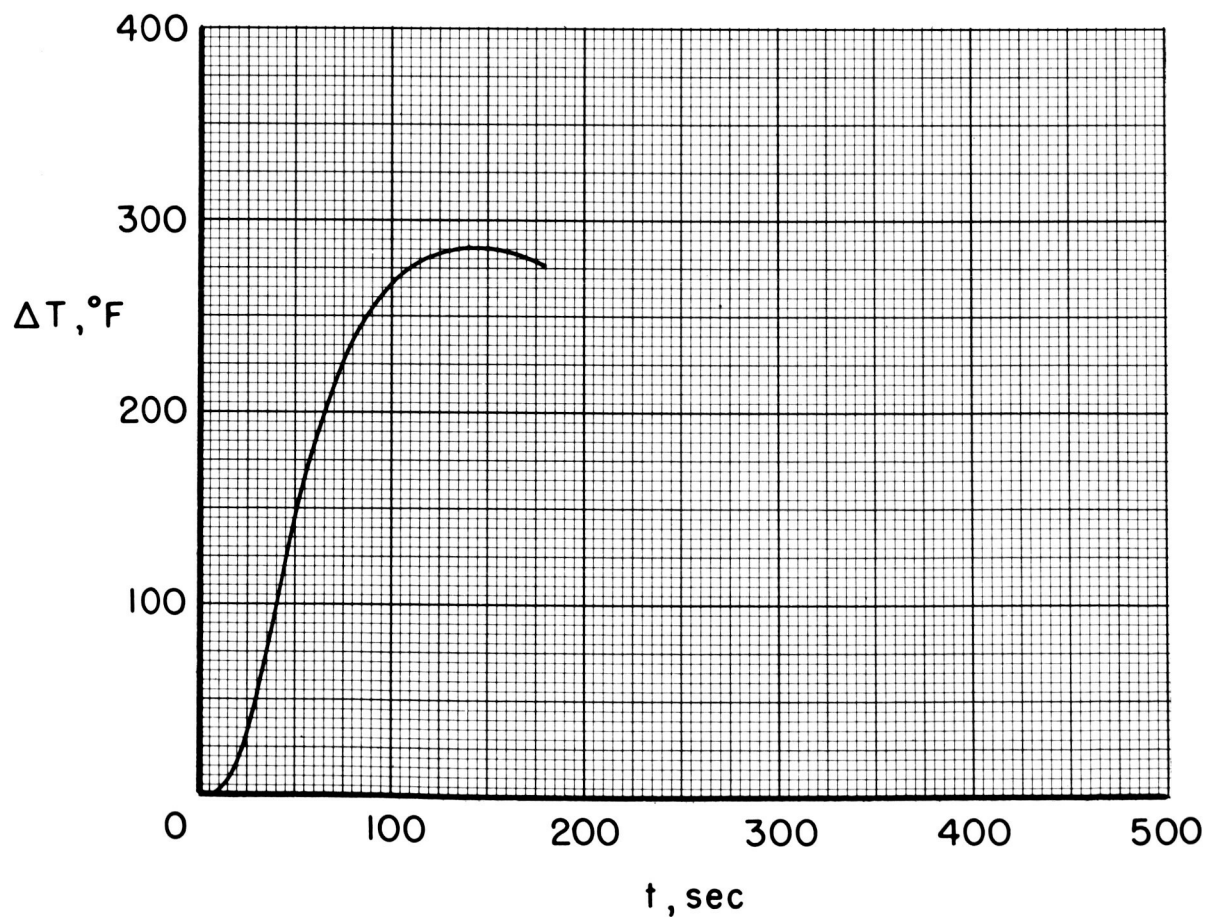


Figure 26.- Material number 19 (Fiberite MX-1344-67).



DECLASSIFIED

Composition

Phenolic resin

Silica fabric

Mineral filler

Density = 111 lb/ft³

Wt. Loss = 8 %

$\Delta T_{\max} = 306 \text{ to } 309^{\circ}\text{F}$

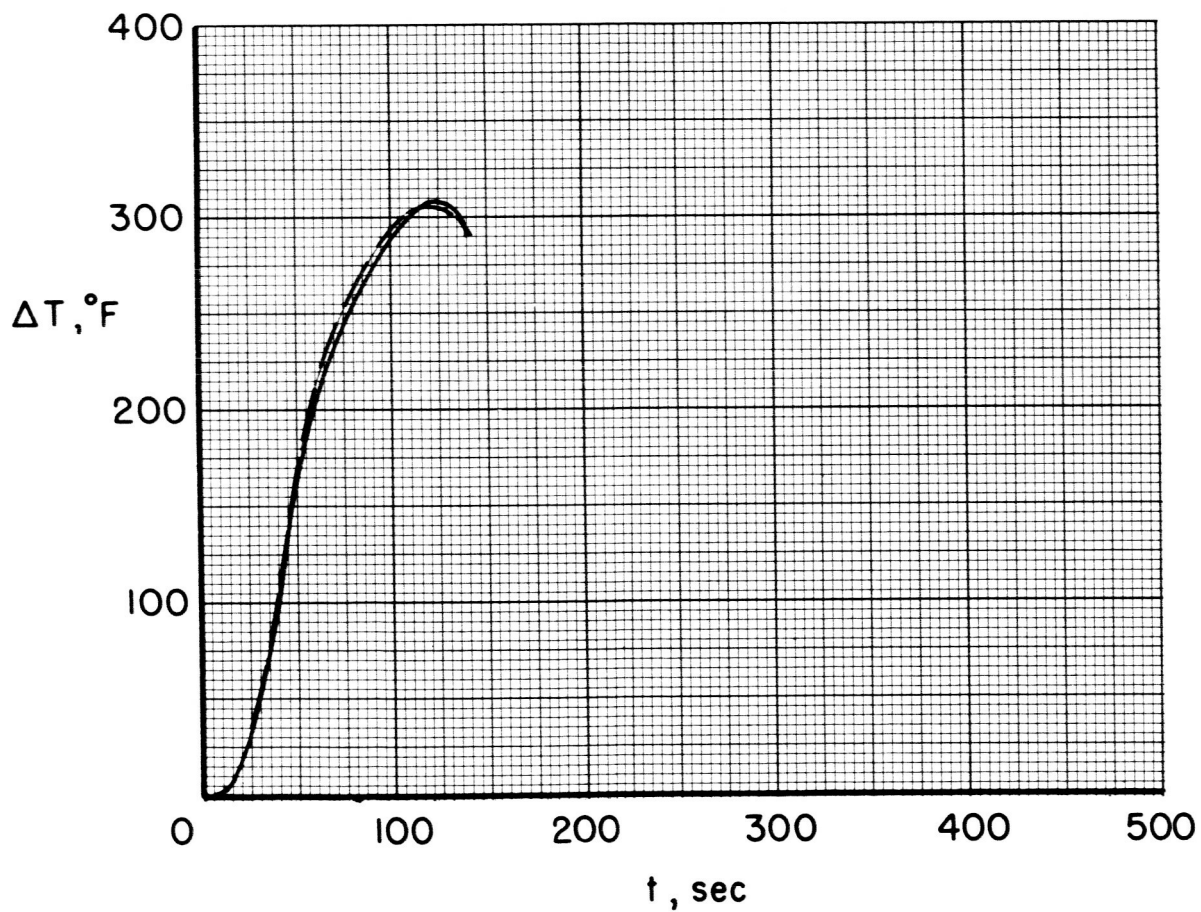
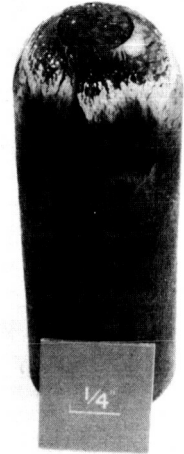
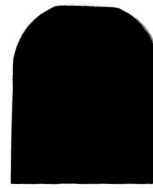
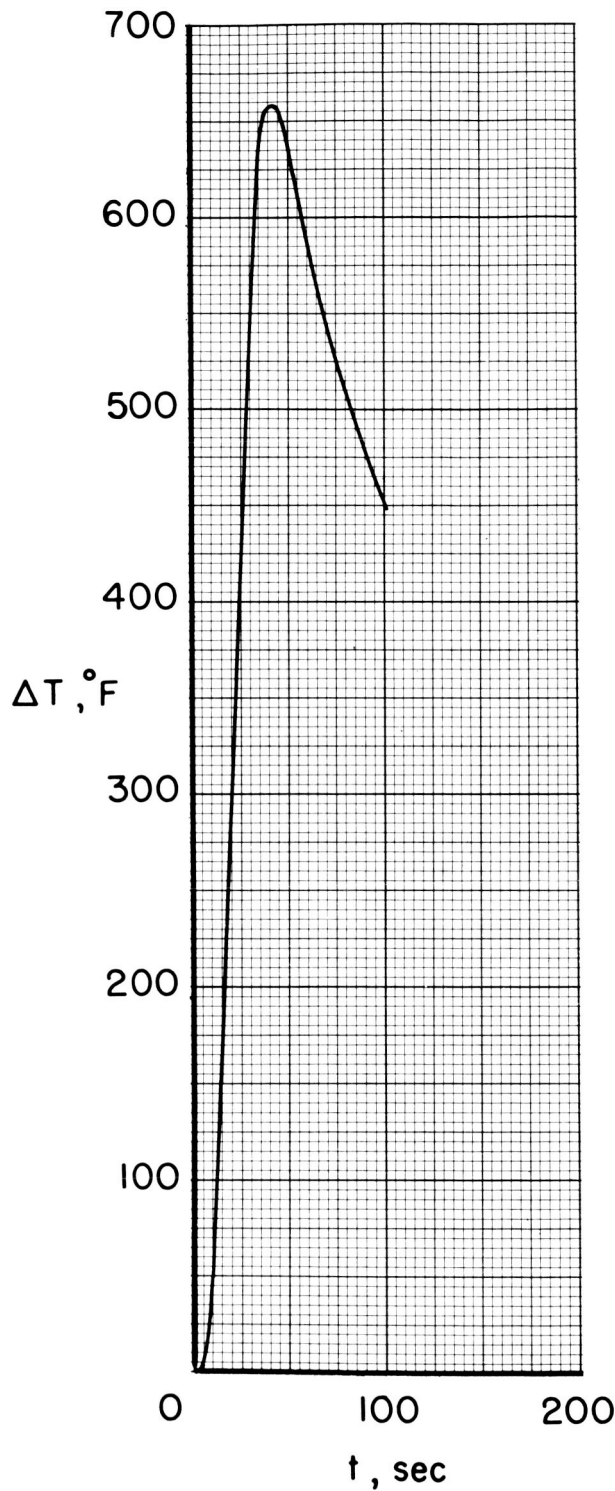


Figure 27.- Material number 20 (Fiberite MX-2625).

03712501030



Composition

Phenolic resin
Graphite fabric
Mineral filler

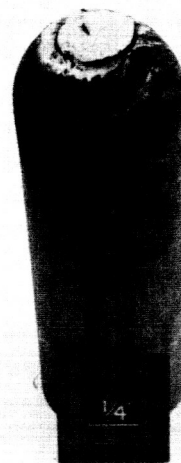
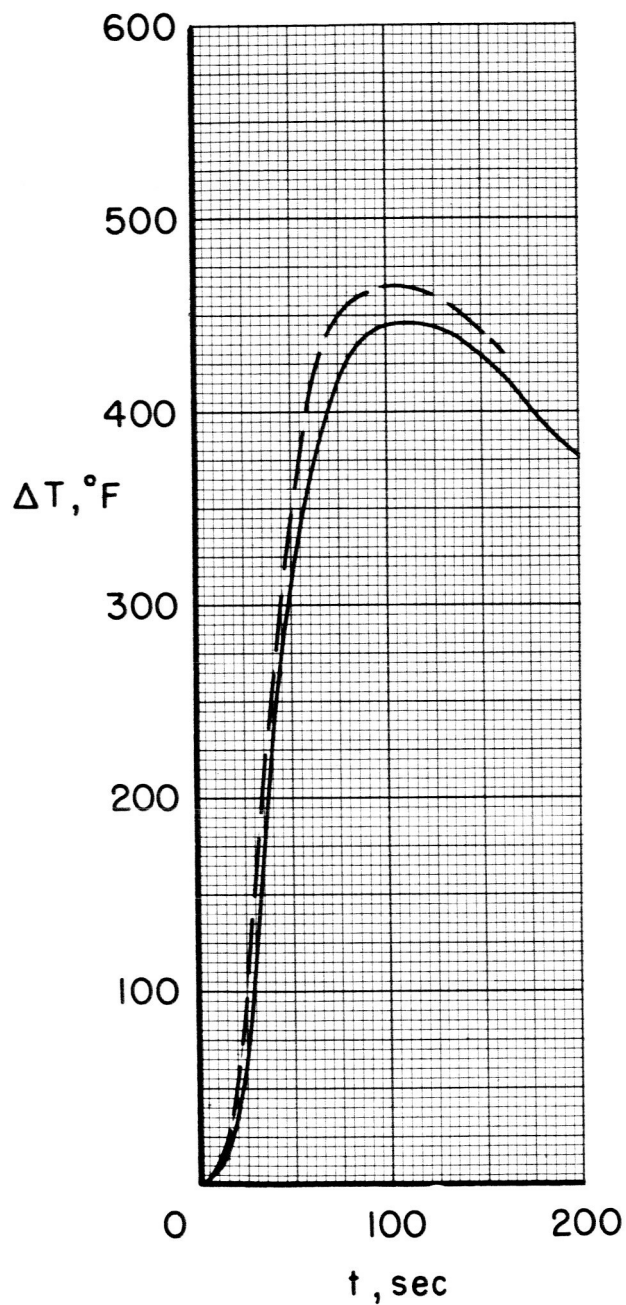
Density = 92 lb/ft³

Wt. Loss = 20 %

$\Delta T_{\max} = 657 ^\circ F$

Figure 28.- Material number 21 (Fiberite MX-2630A).

DECLASSIFIED



Composition

Phenolic resin

Silica fabric

Density = 114 lb/ft³

Wt. Loss = 9 %

ΔT_{\max} = 445 to 464 °F

Figure 29.- Material number 22 (Fiberite MX-2646).

0317254030

Composition

Phenolic resin

Quartz fabric

Density = 110 lb/ft³

Wt. Loss = 13 %

$\Delta T_{\max} = 357^{\circ}\text{F}$

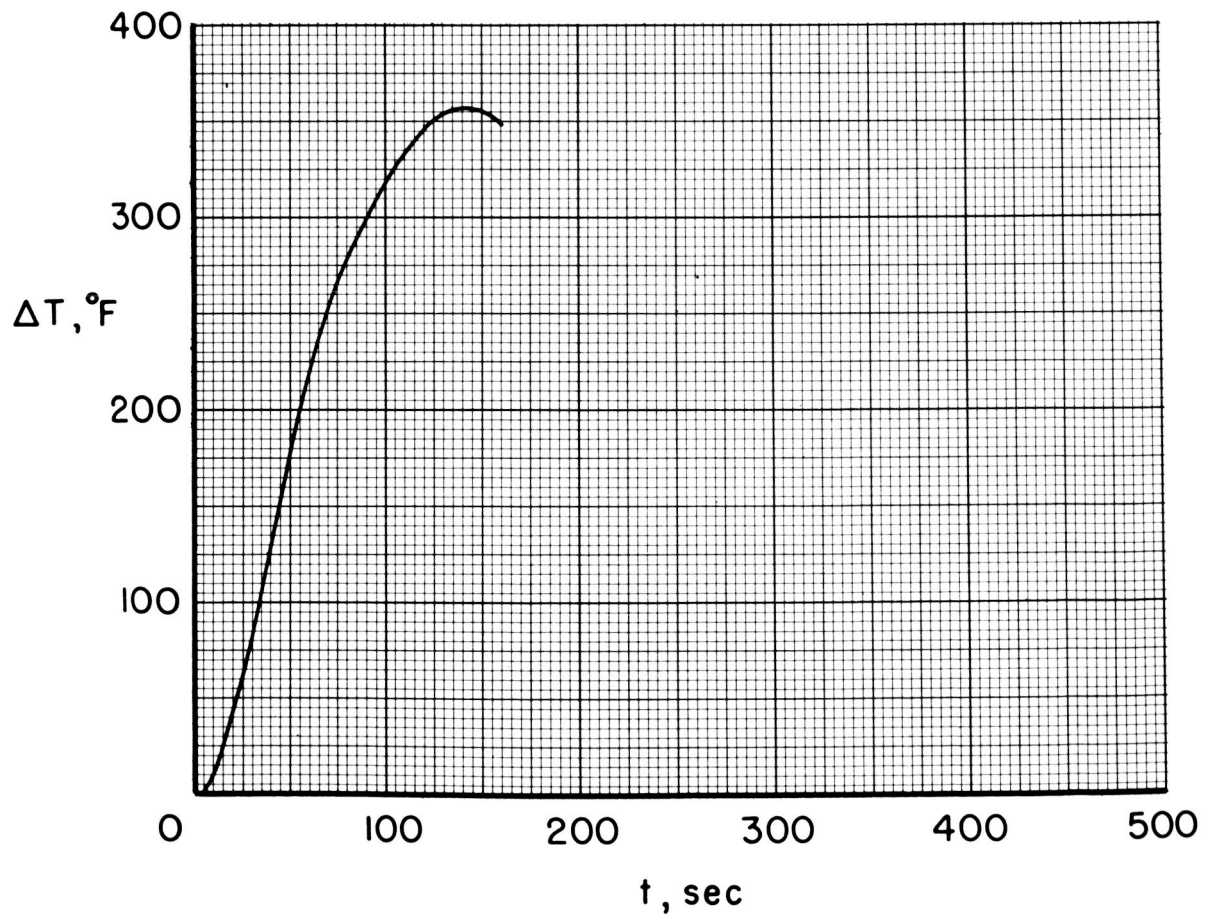
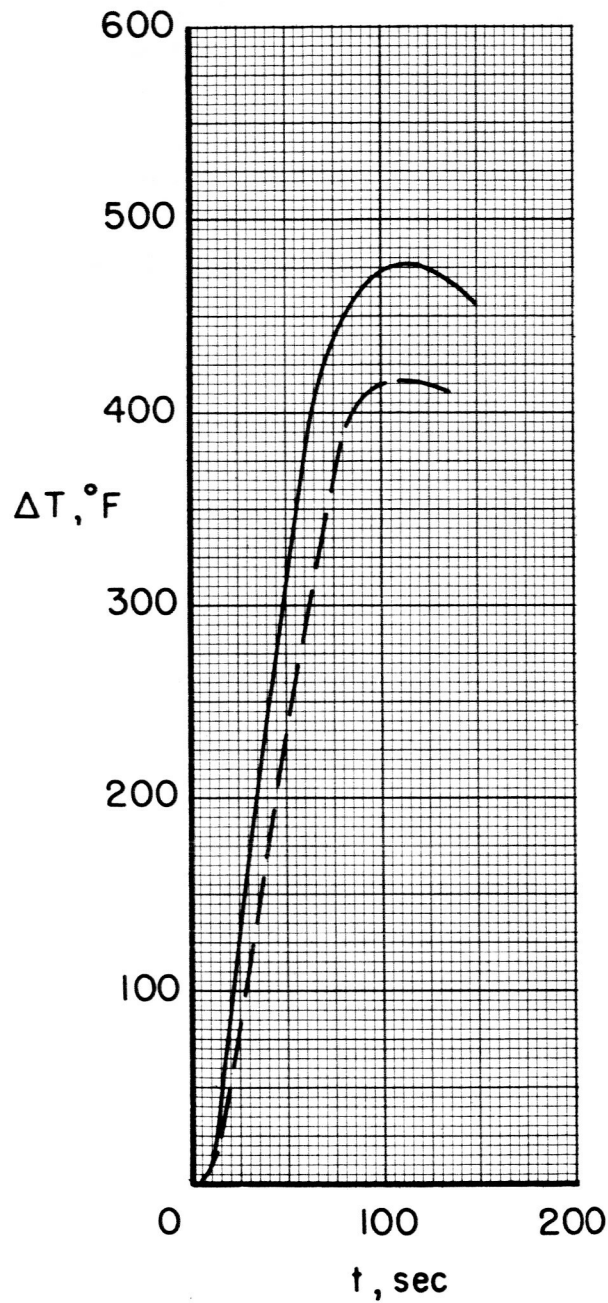


Figure 30.- Material number 23 (Fiberite MX-3581).

DECLASSIFIED



Composition

Phenolic resin

Carbon fibers

Density = 86 lb/ft³

Wt. Loss = 18 %

$\Delta T_{\max} = 417 \text{ to } 477 \text{ }^{\circ}\text{F}$

Figure 31.- Material number 24 (Fiberite MX-4925).

0317-29.030

Composition

Phenolic resin

Nylon flock

Density = 75 lb/ft³

Wt. Loss = 14 %

$\Delta T_{max} = 155^{\circ}F$

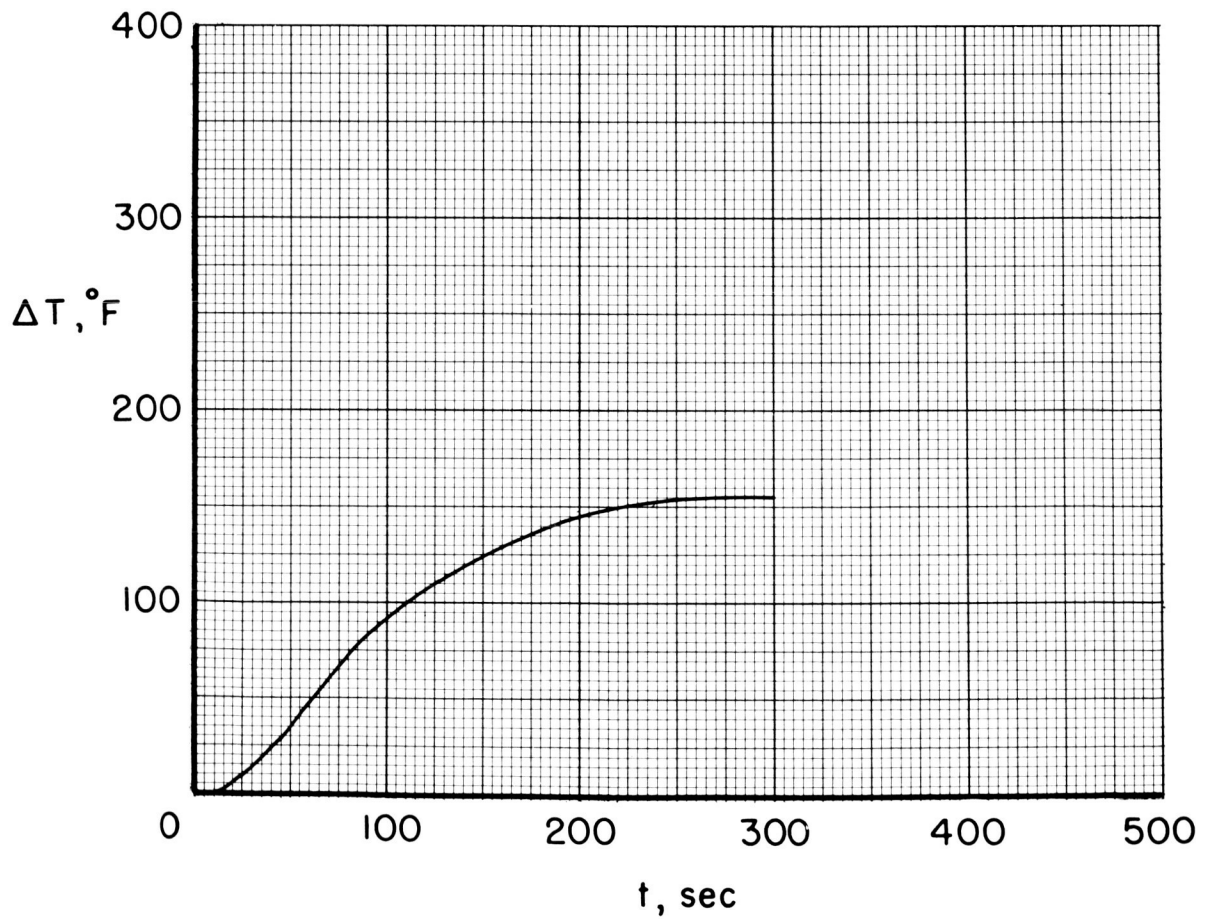


Figure 32.- Material number 25 (Fiberite MX-5675).

~~DECLASSIFIED~~

Composition

Phenolic resin

Nylon roving

Density = 75 lb/ft³

Wt. Loss = 14 %

$\Delta T_{\max} = 134$ to 135°F

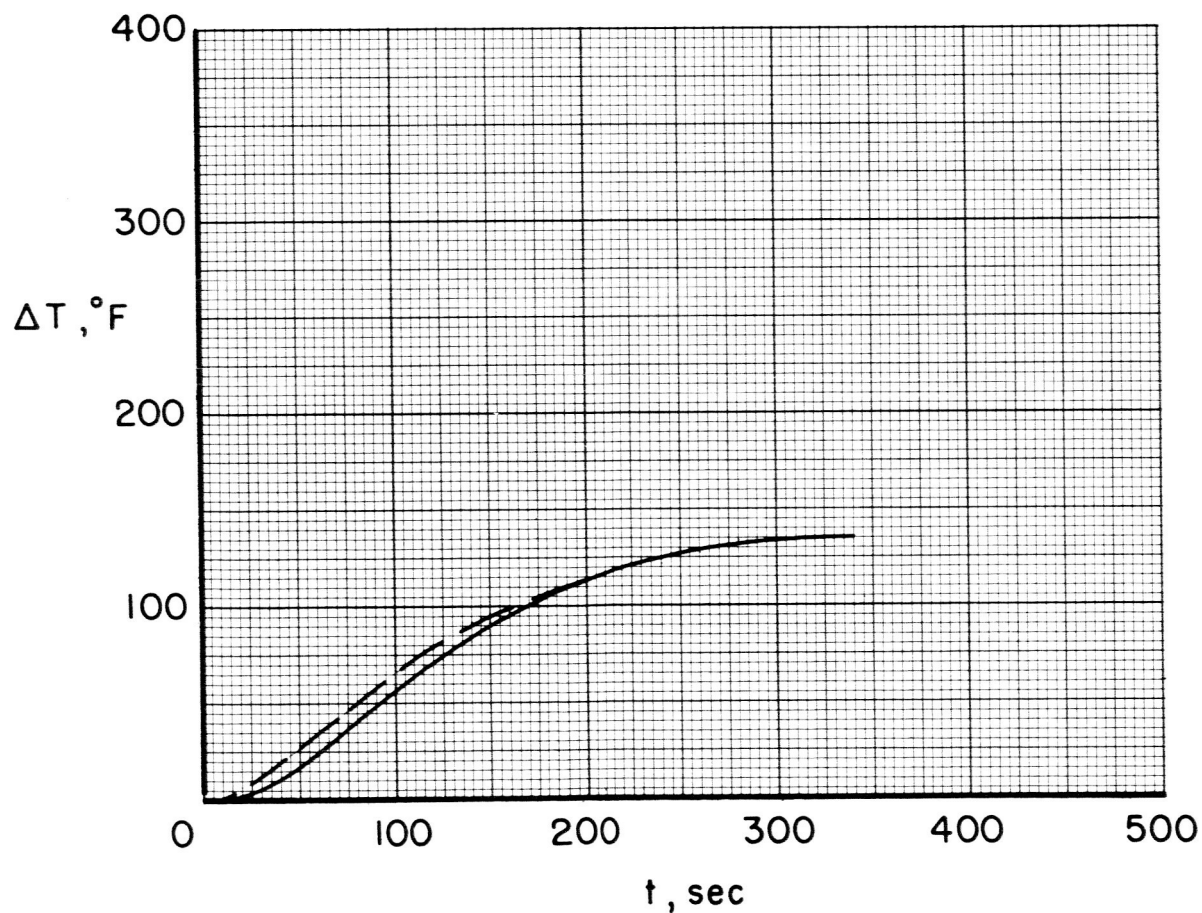


Figure 33.- Material number 26 (Fiberite MX-5683).

~~DECLASSIFIED~~

037129039

Composition

Phenolic resin
Phenolic microballoons
Asbestos

Density = 43 lb/ft³

Wt. Loss = 13 %

ΔT_{\max} = 129 to 153 °F

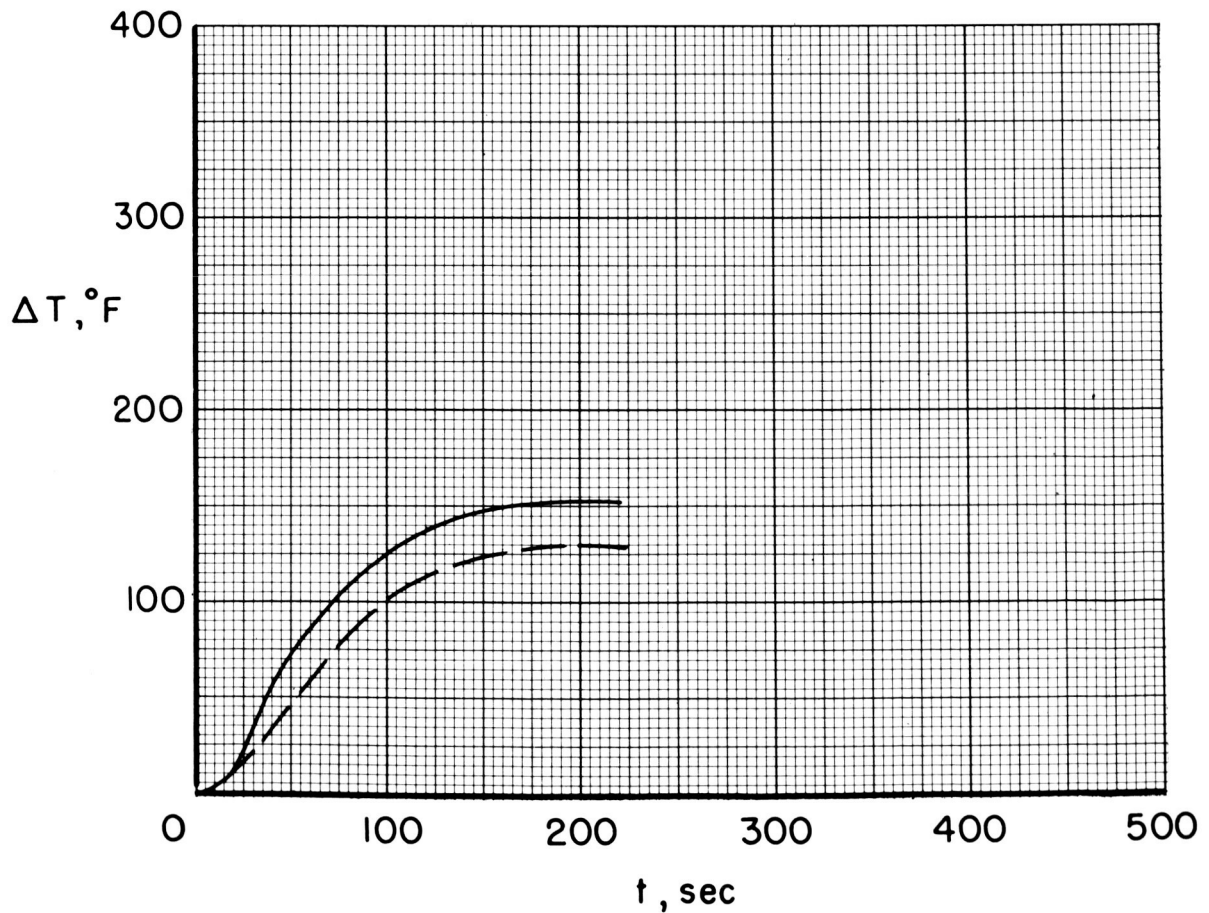


Figure 34.- Material number 27 (Fiberite MX-5700).

REF ID: A609780

Composition

Phenolic resin
Phenolic microballoons
Nylon



Density = 62 lb/ft³

Wt. Loss = 13 %

$\Delta T_{\max} = 126$ to 131°F

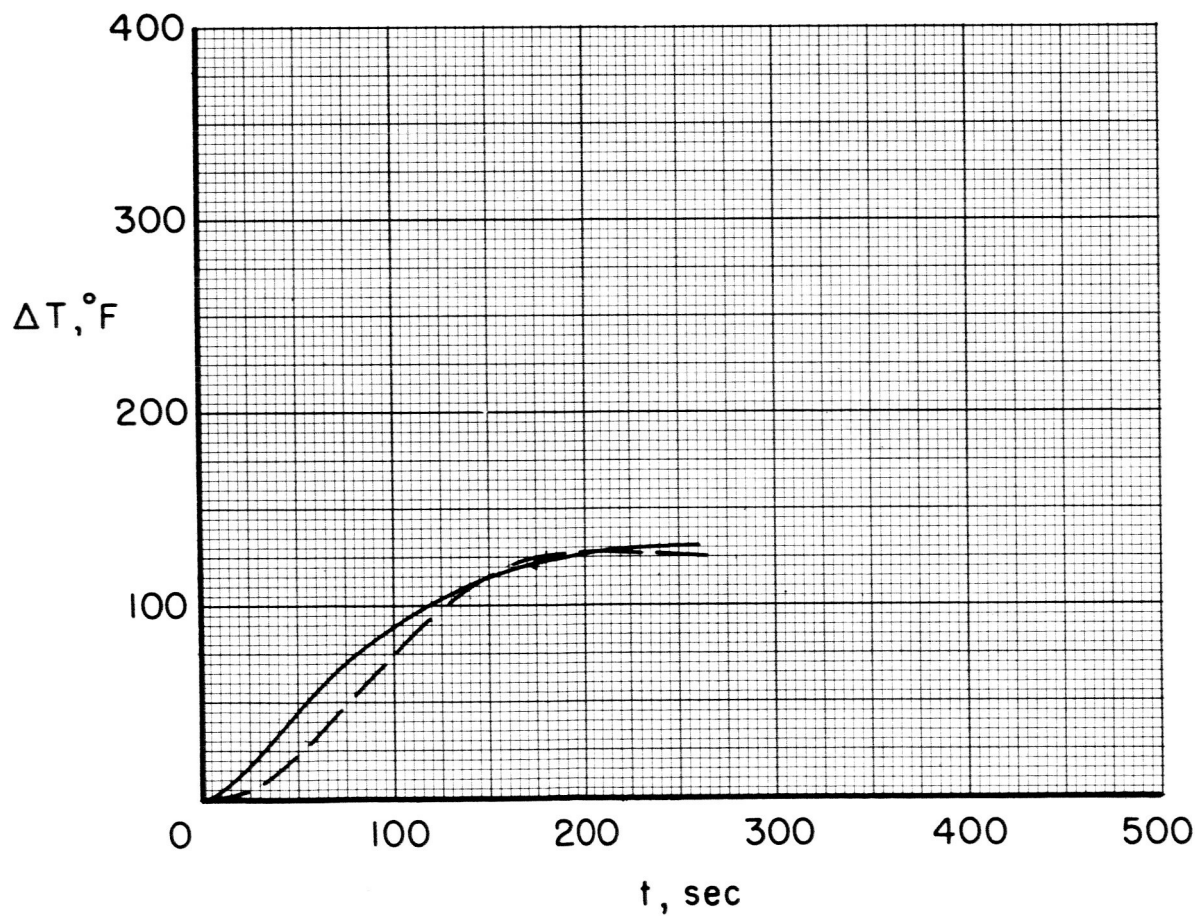
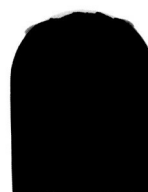
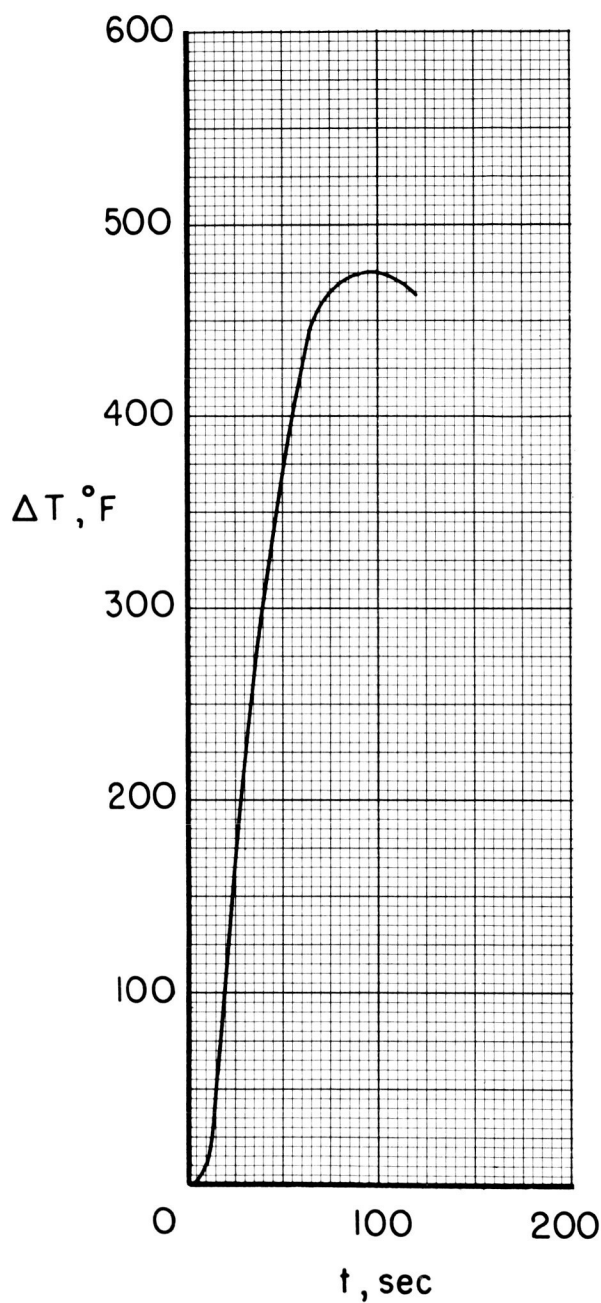


Figure 35.- Material number 28 (Fiberite MX-7500).



Composition

Phenolic resin

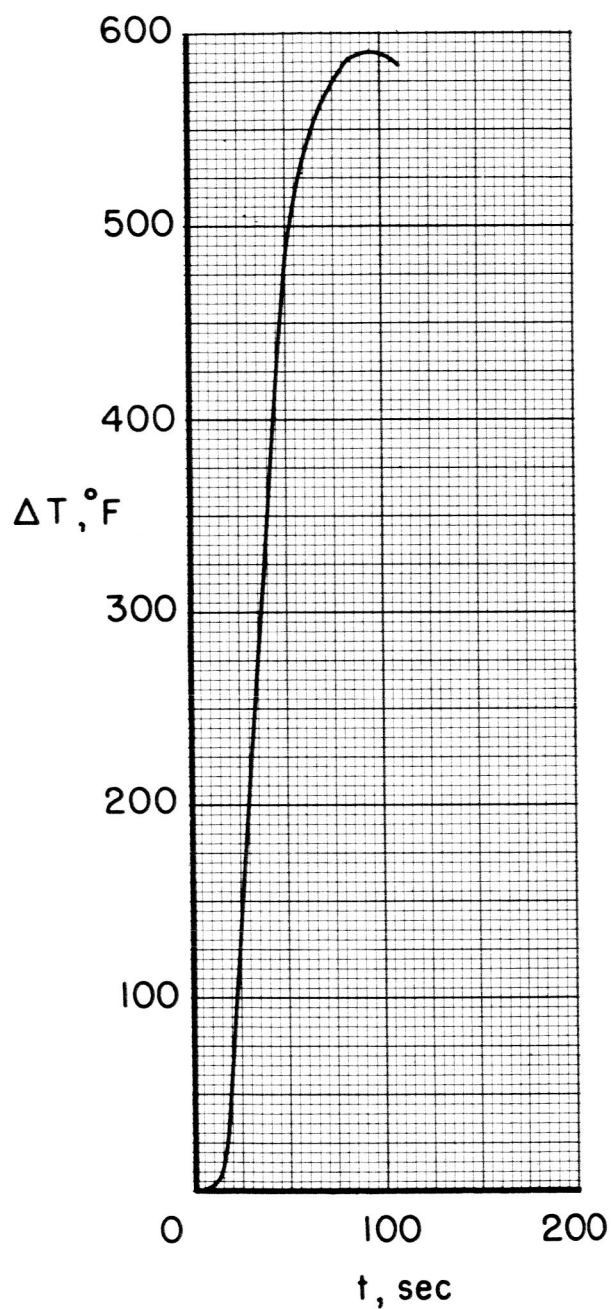
Asbestos

Density = 110 lb/ft³

Wt. Loss = 17 %

$\Delta T_{max} = 476 ^\circ F$

Figure 36.- Material number 29 (R.M. 150 - RPD).



Composition

Phenolic resin

Nylon

Asbestos

Graphite

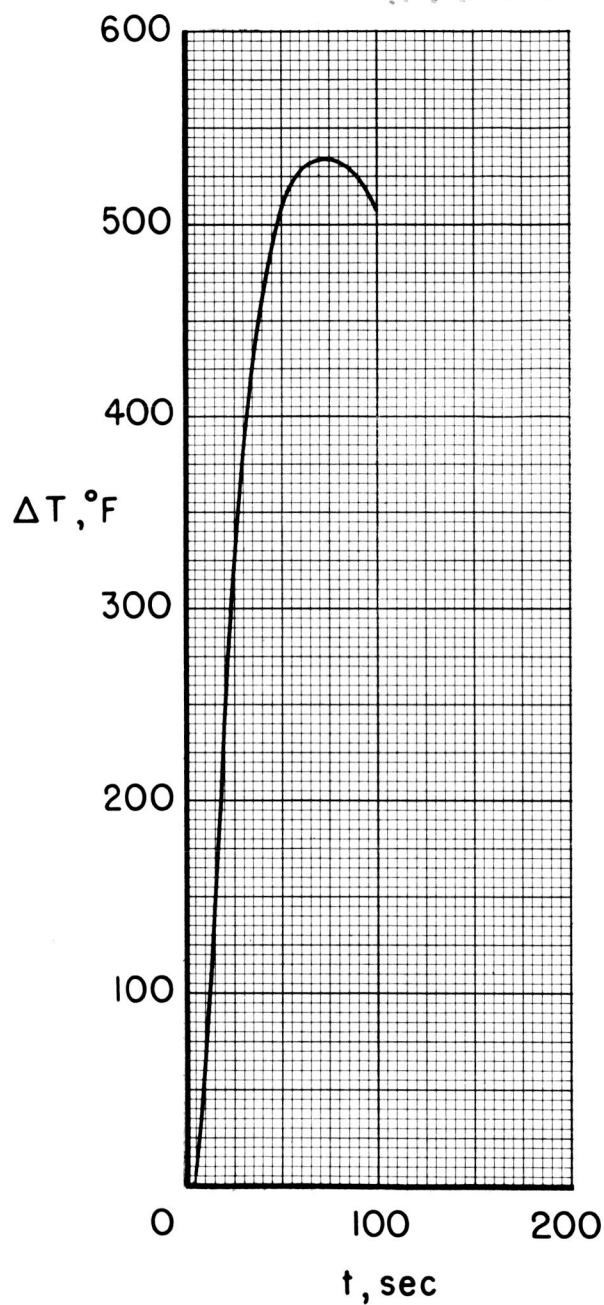
Density = 98 lb/ft³

Wt. Loss = 19 %

$\Delta T_{\text{max}} = 591 ^\circ\text{F}$

Figure 37.- Material number 30 (R.M. 154 - RPD).

SECRET



Composition

Phenolic-nylon resin

Asbestos

Graphite

Density = 102 lb/ft³

Wt. Loss = 19 %

$\Delta T_{\max} = 532 ^\circ F$

Figure 38.- Material number 31 (R.M. 155 - RPD).

CONFIDENTIAL

Composition

Phenolic resin

Glass fibers

Density = 116 lb/ft³

Wt. Loss = 18 %

$\Delta T_{\max} = 334^{\circ}\text{F}$

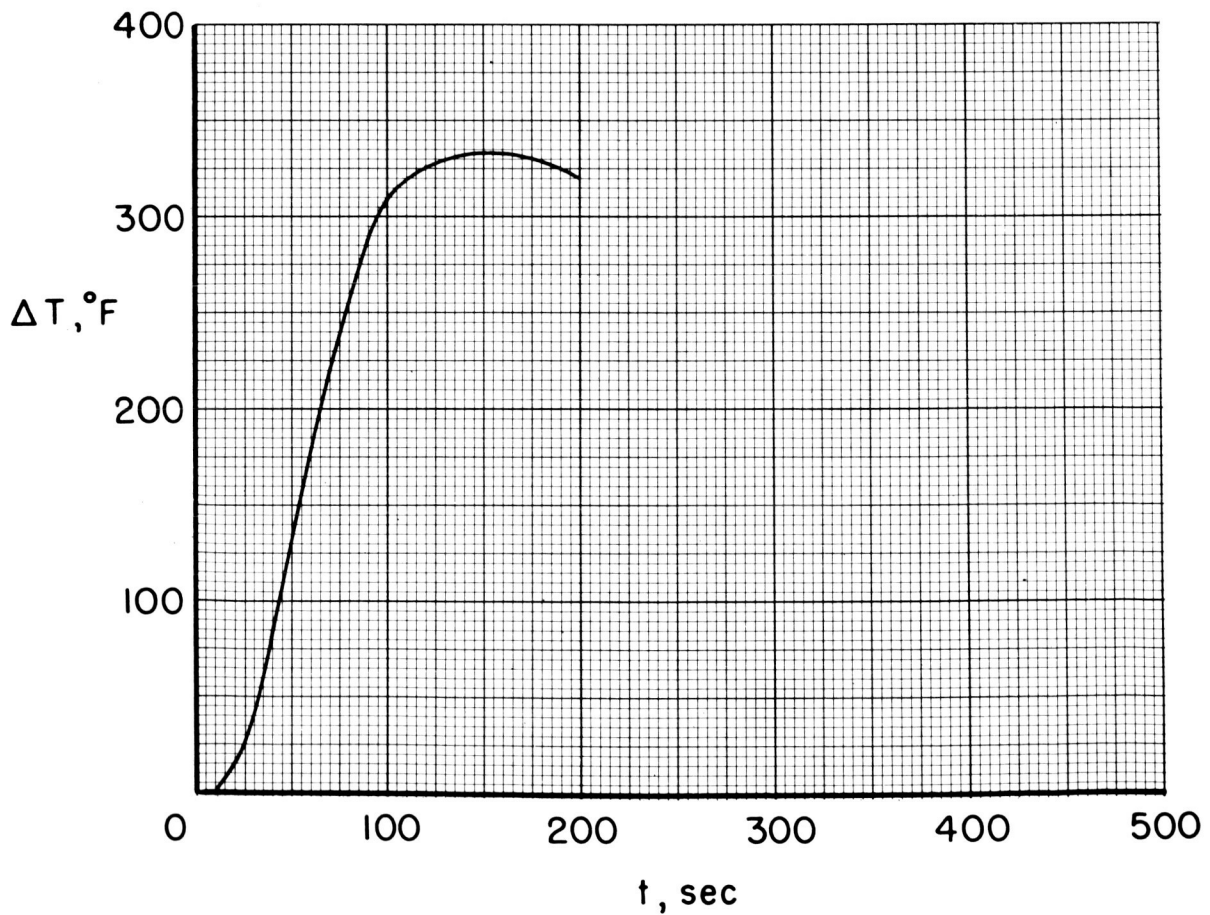
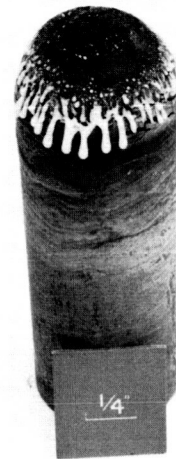


Figure 40.- Material number 33 (91-LD).

CONFIDENTIAL

~~CONFIDENTIAL~~

Composition

Phenolic resin

Silica fabric

Density = 96 lb/ft³

Wt. Loss = 8 %

$\Delta T_{\max} = 376$ to 392 °F

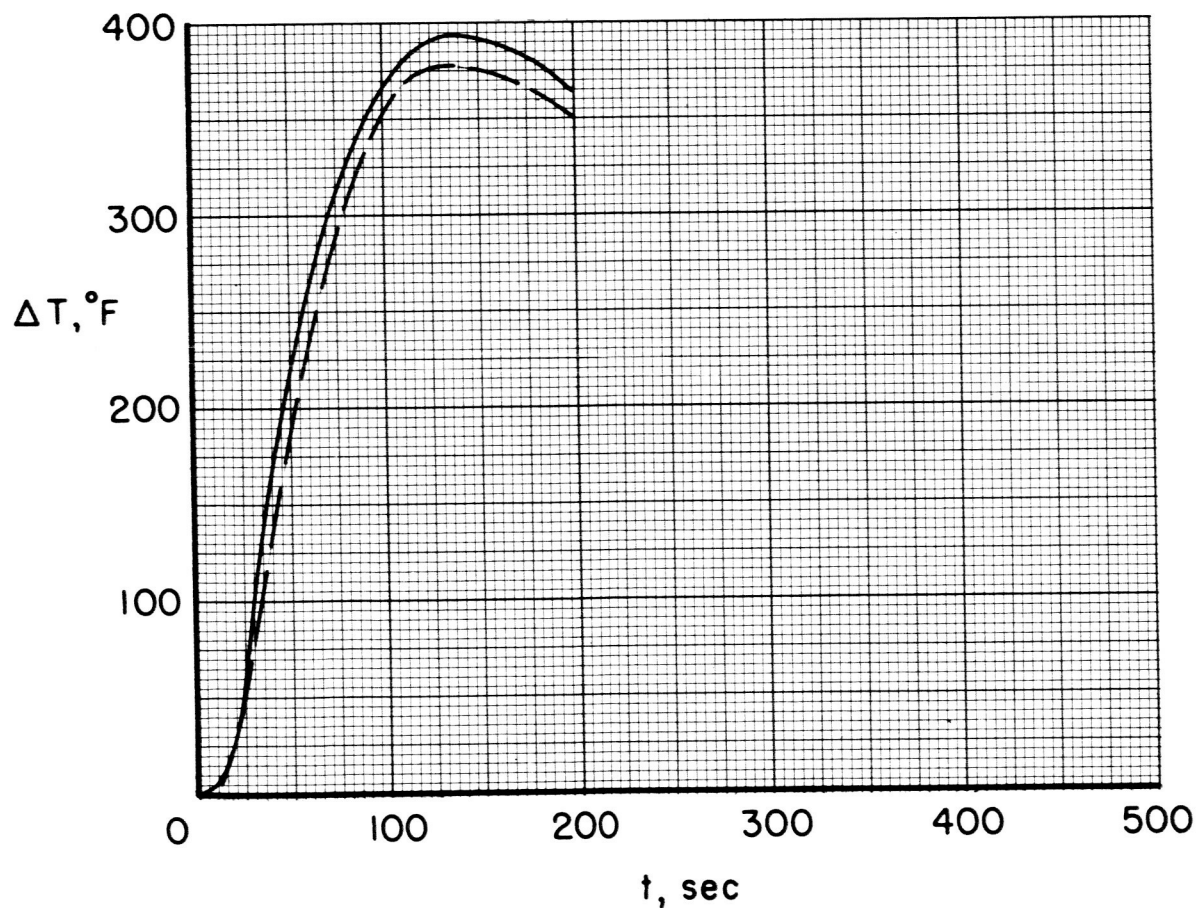


Figure 41.- Material number 34 (Astrolite).

~~CONFIDENTIAL~~

CONFIDENTIAL

Composition

Phenolic resin

Cotton fabric

Density = 87 lb/ft³

Wt. Loss = 18 %

ΔT_{\max} = 176 to 199 °F

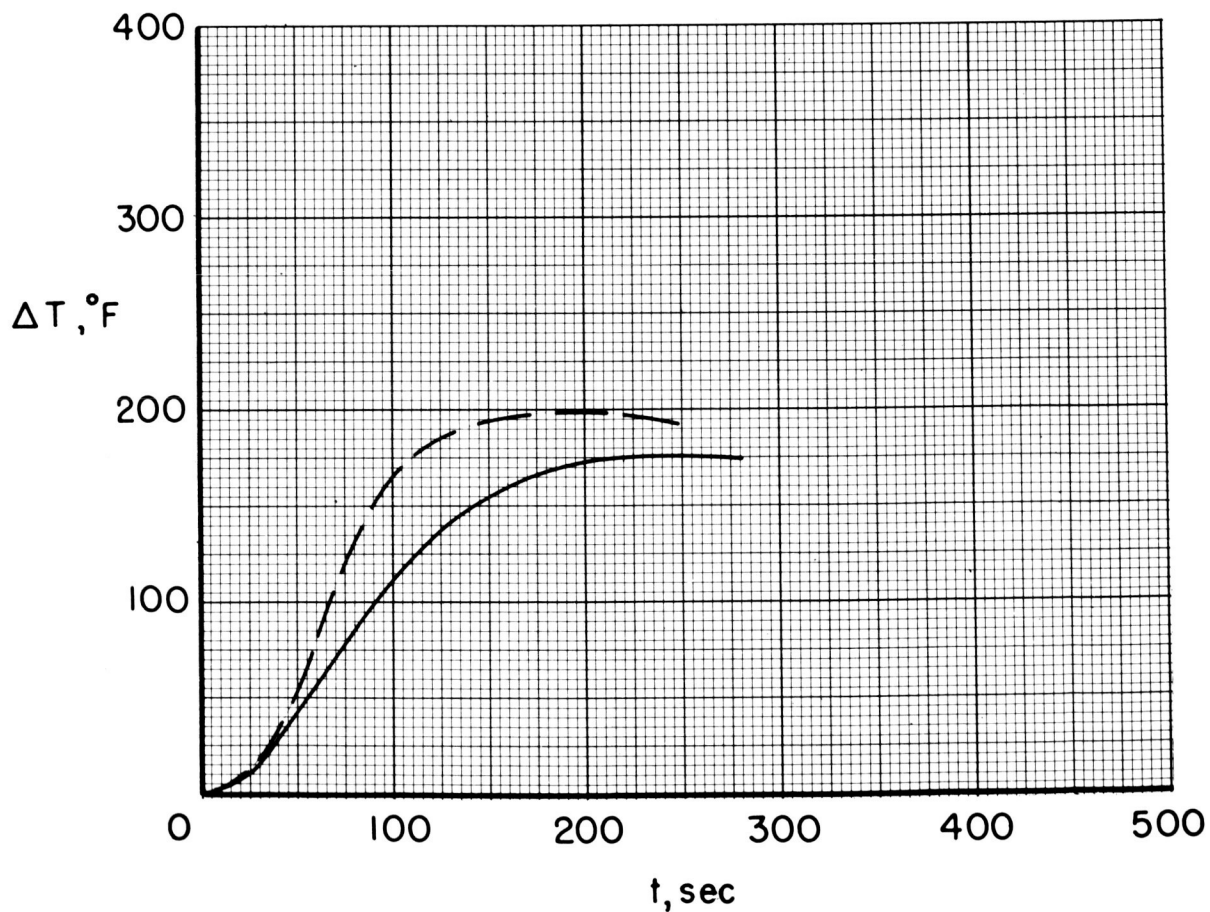
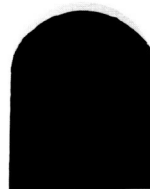


Figure 42.- Material number 35 (Bakelite).

~~SECRET~~

Composition

Polyethylene resin

Carbon black

Density = 60 lb/ft³

Wt. Loss = 32 %

$\Delta T_{\max} = 101^{\circ}\text{F}$

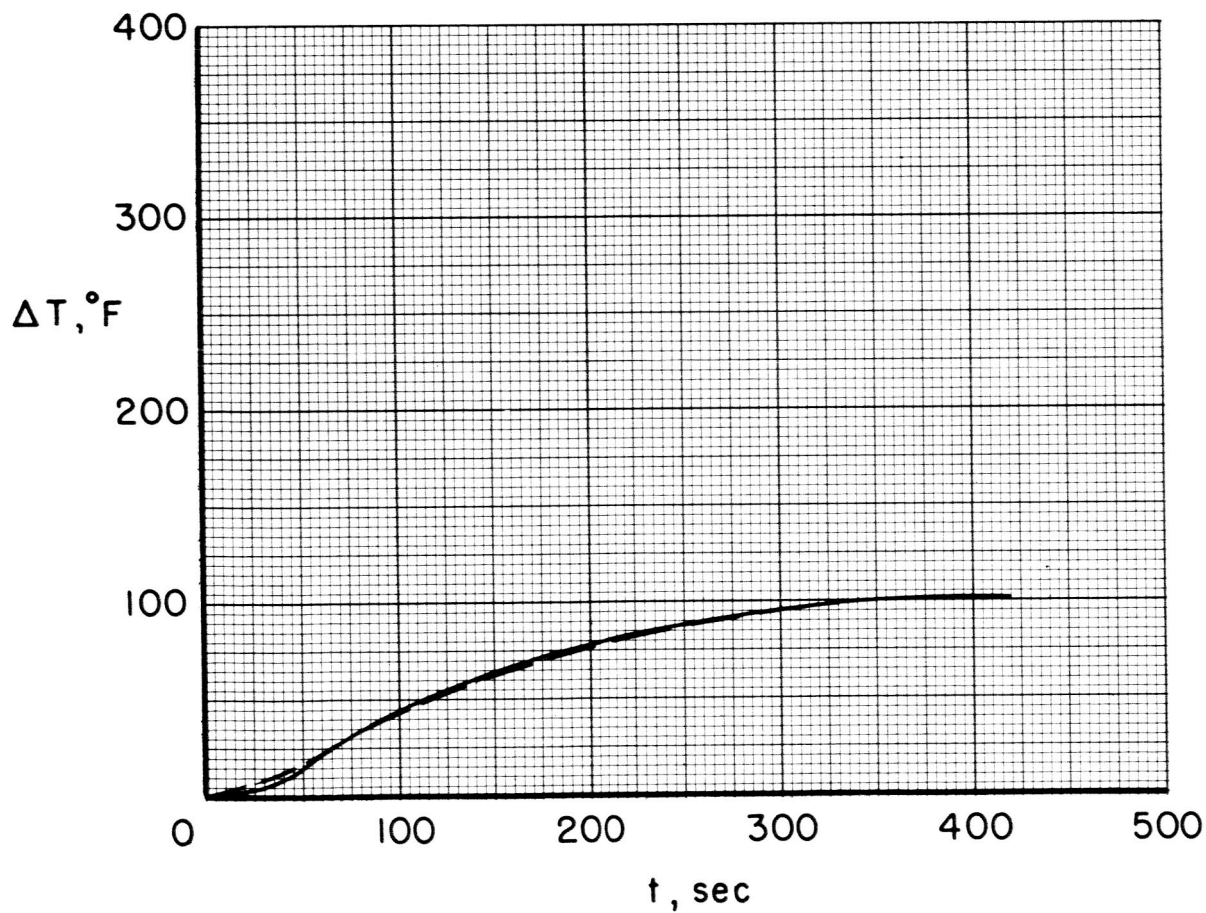
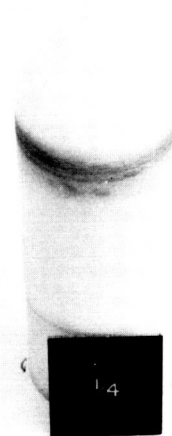
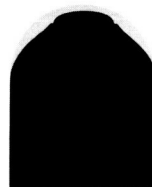
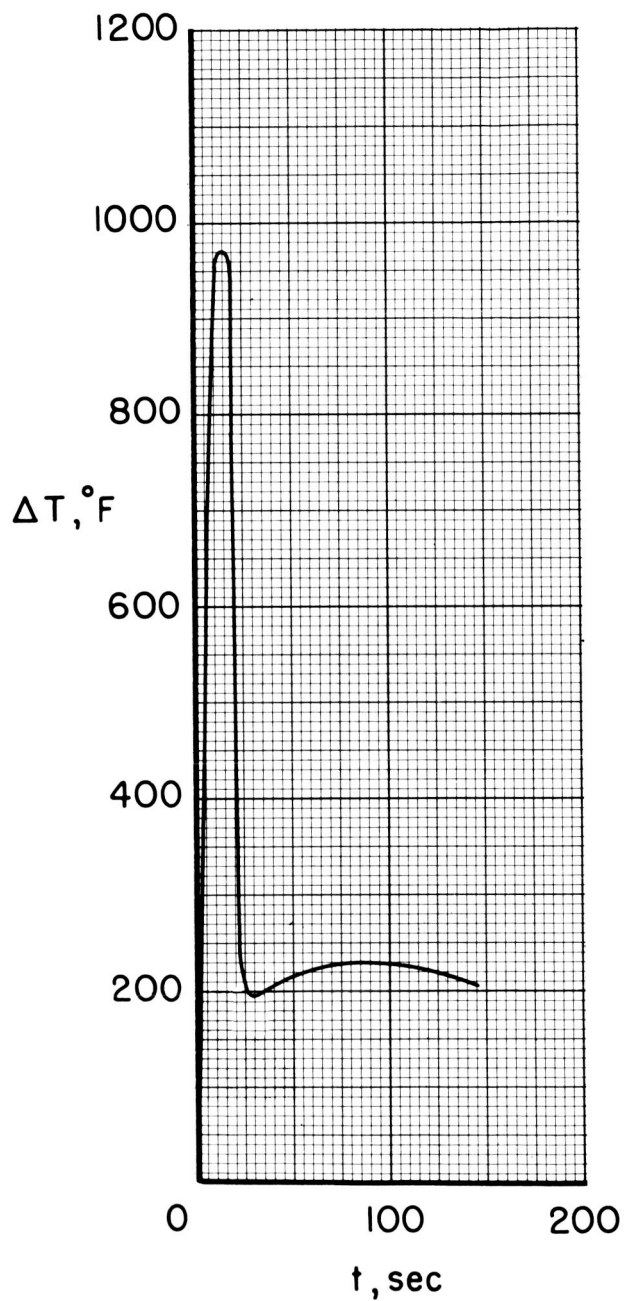


Figure 43.- Material number 36 (Fortiflex).

0371030



Composition

Polytetrafluoro-
ethylene

Density = 136 lb/ft³

Wt. Loss = 31 %

$\Delta T_{\text{max}} = 970 ^\circ\text{F}$

Figure 44.- Material number 37 (White Teflon).

DECLASSIFIED

Composition

Polytetrafluoro -

ethylene

Graphite

Density = 135 lb/ft³

Wt. Loss = 39 %

$\Delta T_{\max} = 226$ to 230°F

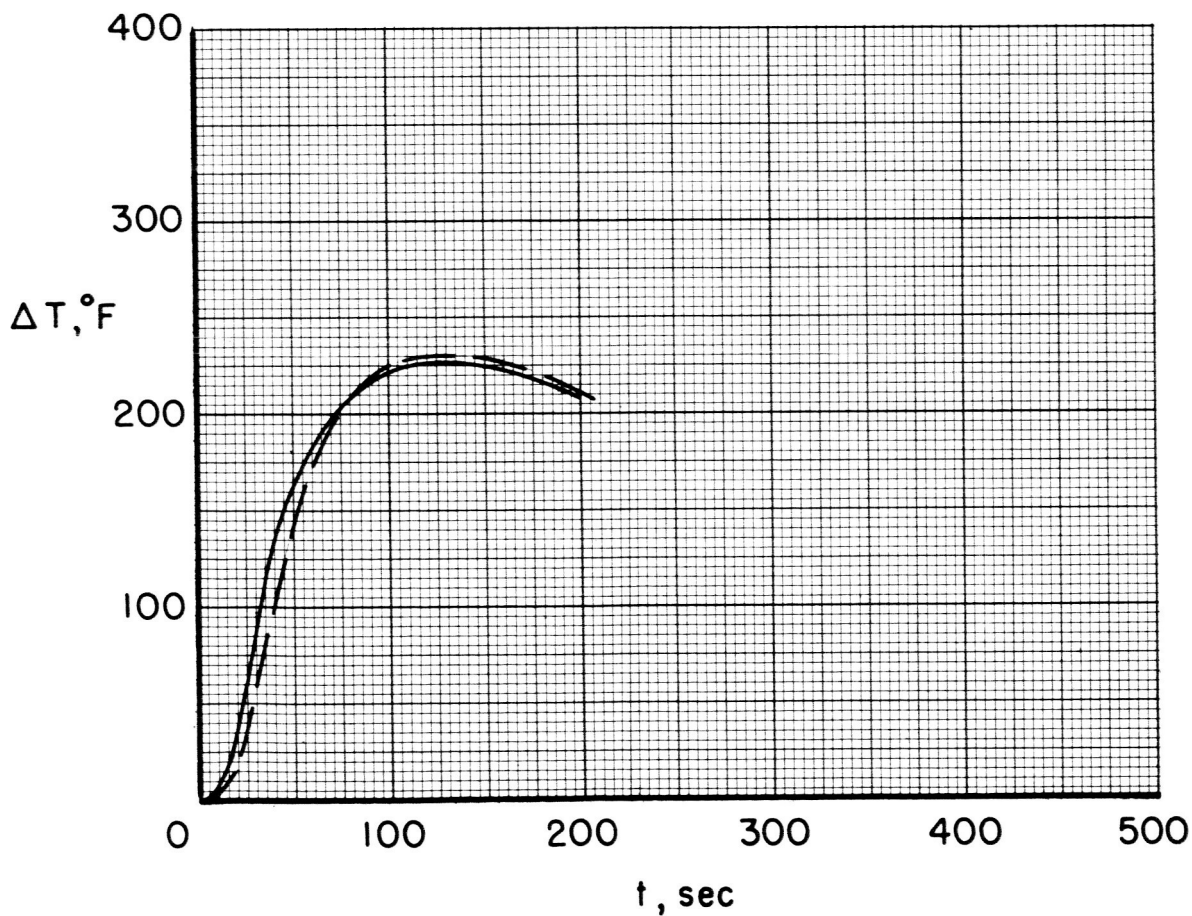


Figure 45.- Material number 38 (Black Teflon).

03710-41030

Composition

Phenolic resin

Nylon

Density = 75 lb/ft³

Wt. Loss = 14 %

$\Delta T_{\max} = 116 \text{ to } 118 ^\circ\text{F}$

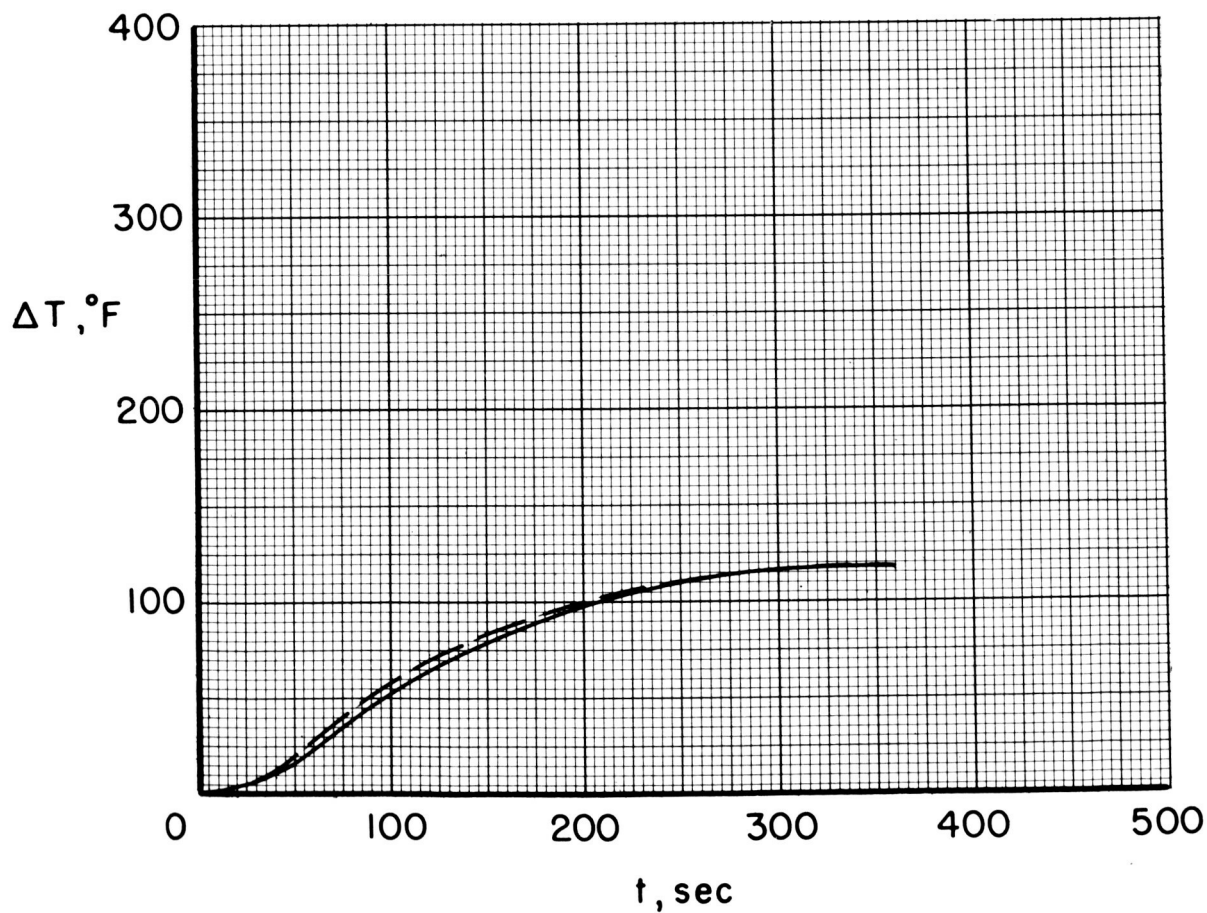


Figure 46.- Material number 39 (High density phenolic-nylon).

~~DECLASSIFIED~~

Composition

Phenolic resin

Phenolic microballoons

Nylon

Density = 46 lb/ft³

Wt. Loss = 11 %

$\Delta T_{\max} = 93^{\circ}\text{F}$

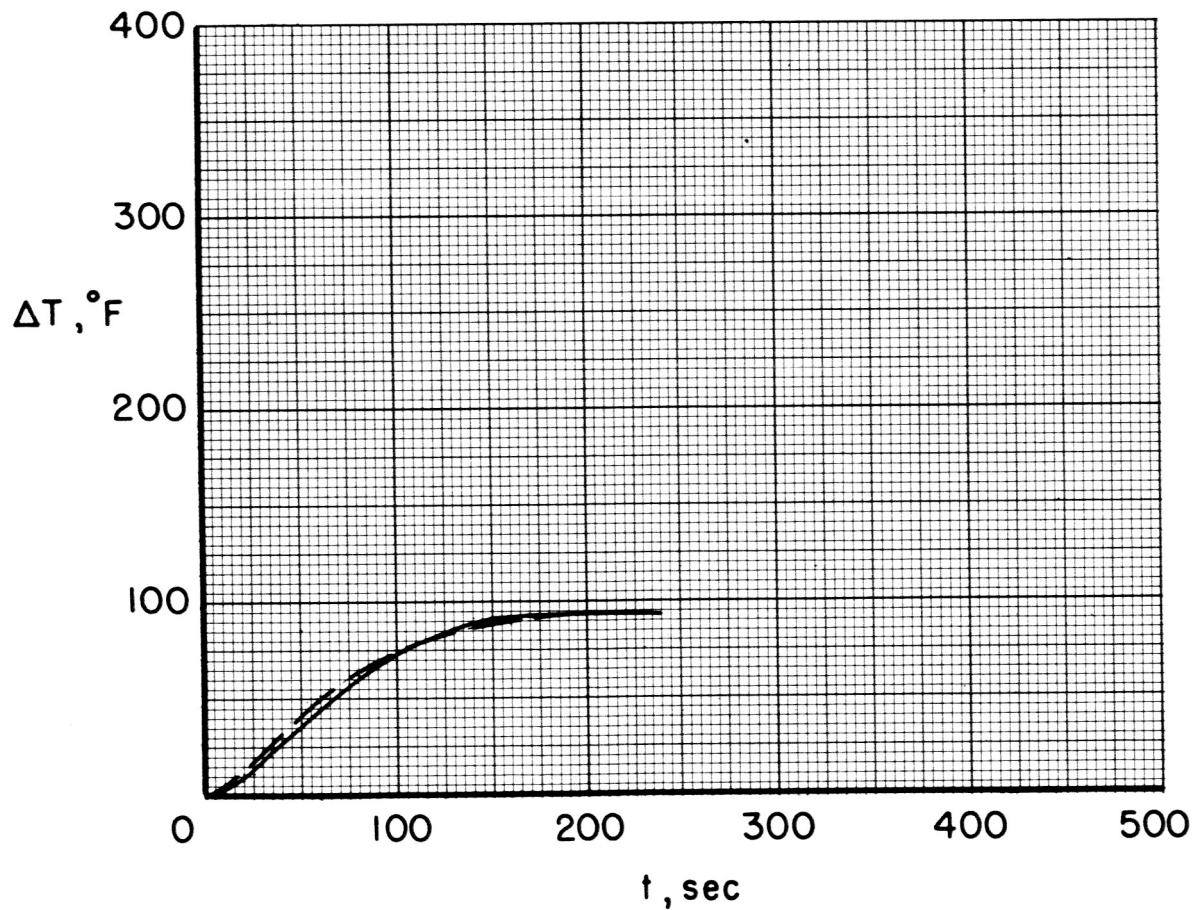
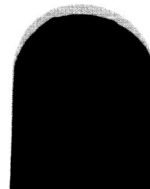
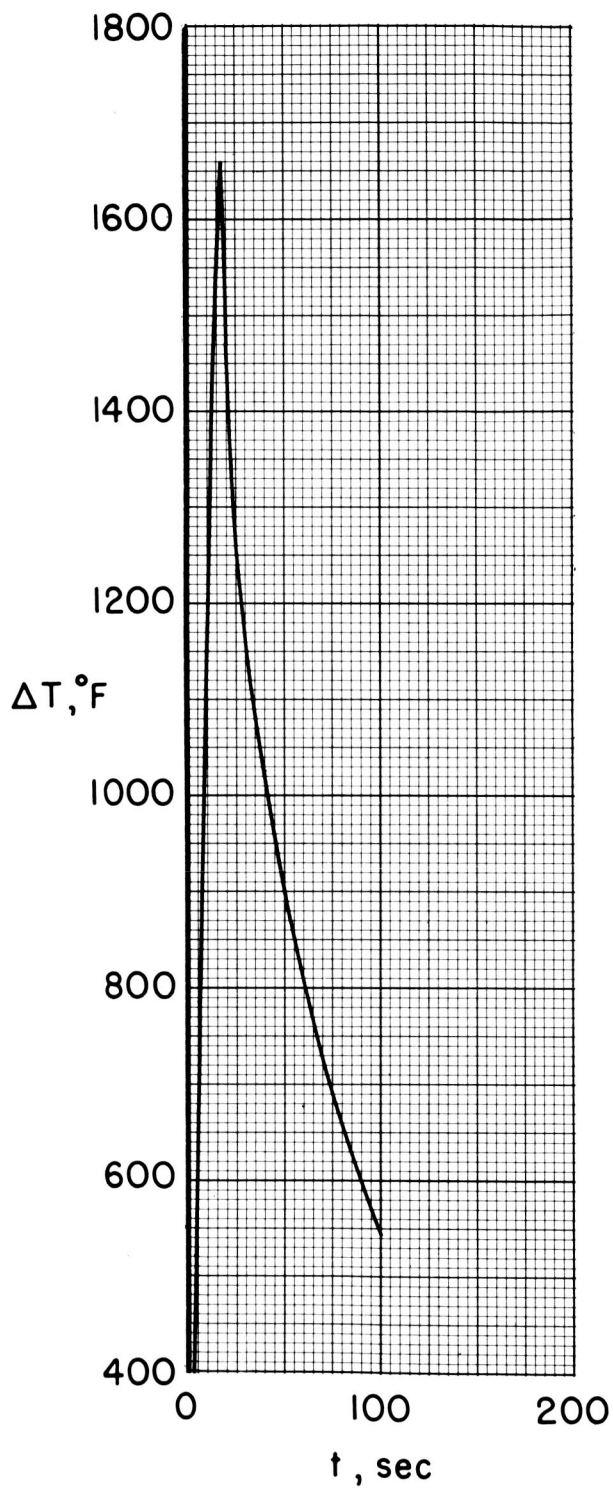


Figure 47.- Material number 40 (Low density phenolic-nylon).

037122030



Composition

Graphite

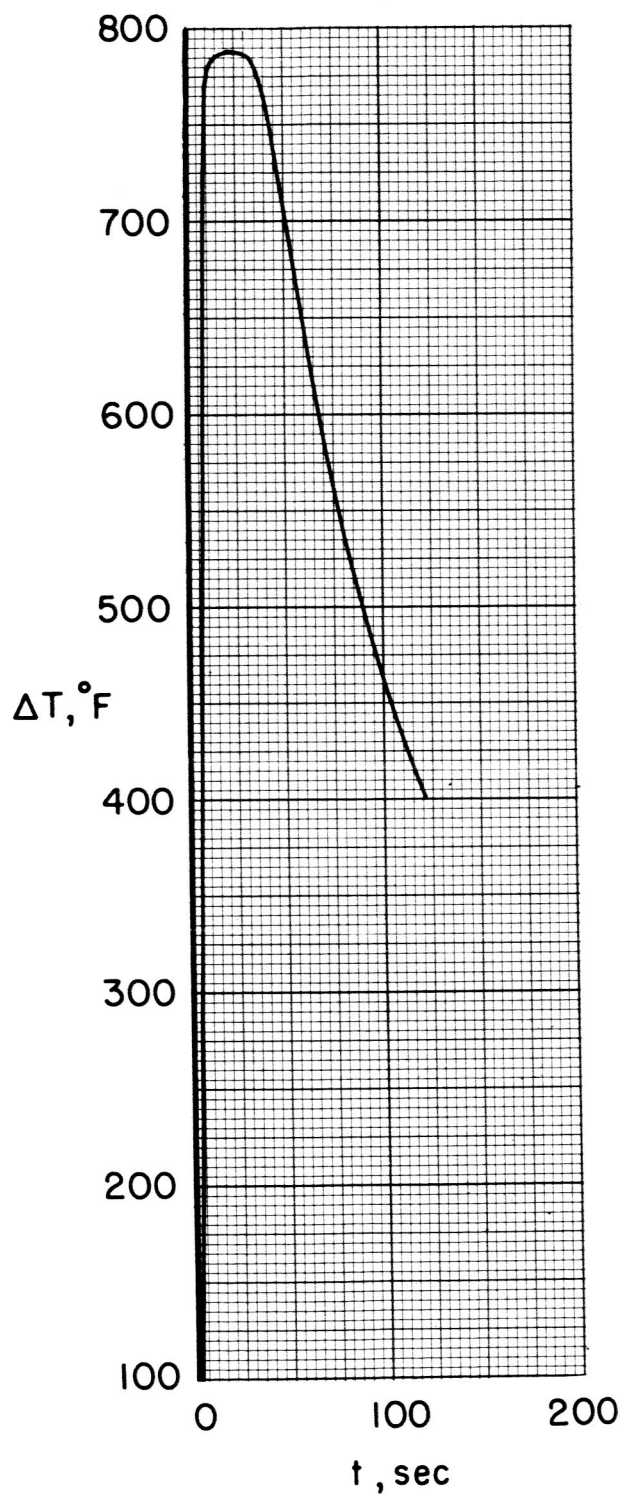
Density = 104 lb/ft³

Wt. Loss = 2 %

$\Delta T_{\max} = 1660 ^\circ F$

Figure 48.- Material number 41 (Graphite).

REF ID: A66484



Composition

Boron nitride

Density = 132 lb/ft³

Wt. Loss = <1.0 %

$\Delta T_{\text{max}} = 791 ^\circ\text{F}$

Figure 49.- Material number 42 (Boron nitride).

Composition

White oak
(kiln dry)

Density = 44 lb/ft³

Wt. Loss = 17 %

$\Delta T_{max} = 65 \text{ to } 71 \text{ }^{\circ}\text{F}$

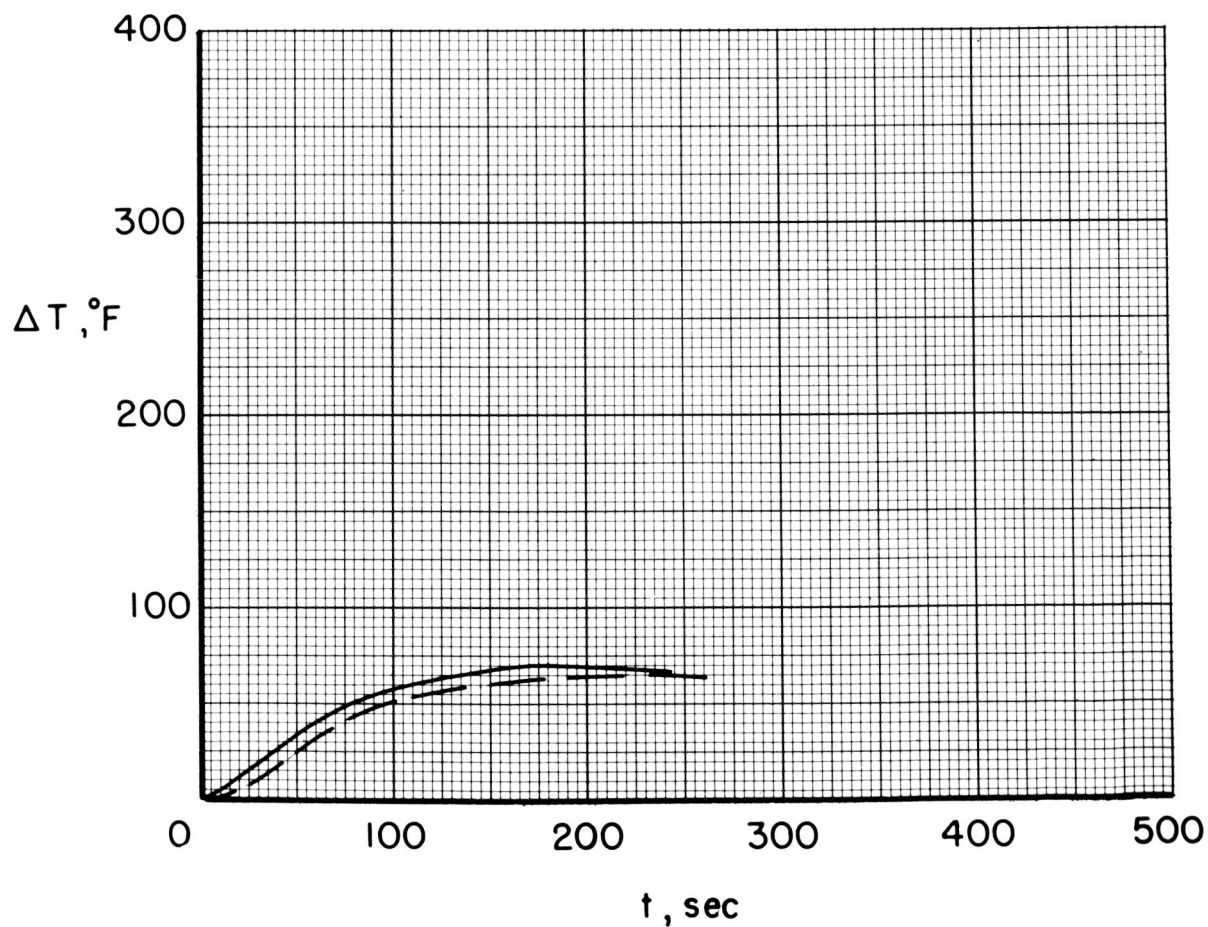


Figure 50.- Material number 43 (Oak wood).

DECLASSIFIED

Composition

Balsa wood

Density = 16 lb/ft³

Wt. Loss = 16 %

$\Delta T_{\max} = 57 \text{ to } 60^\circ\text{F} (2.0 \text{ lb/ft}^2)$

ΔT_{\max} Adjusted for Std.

Wt. = 17 to 19 °F

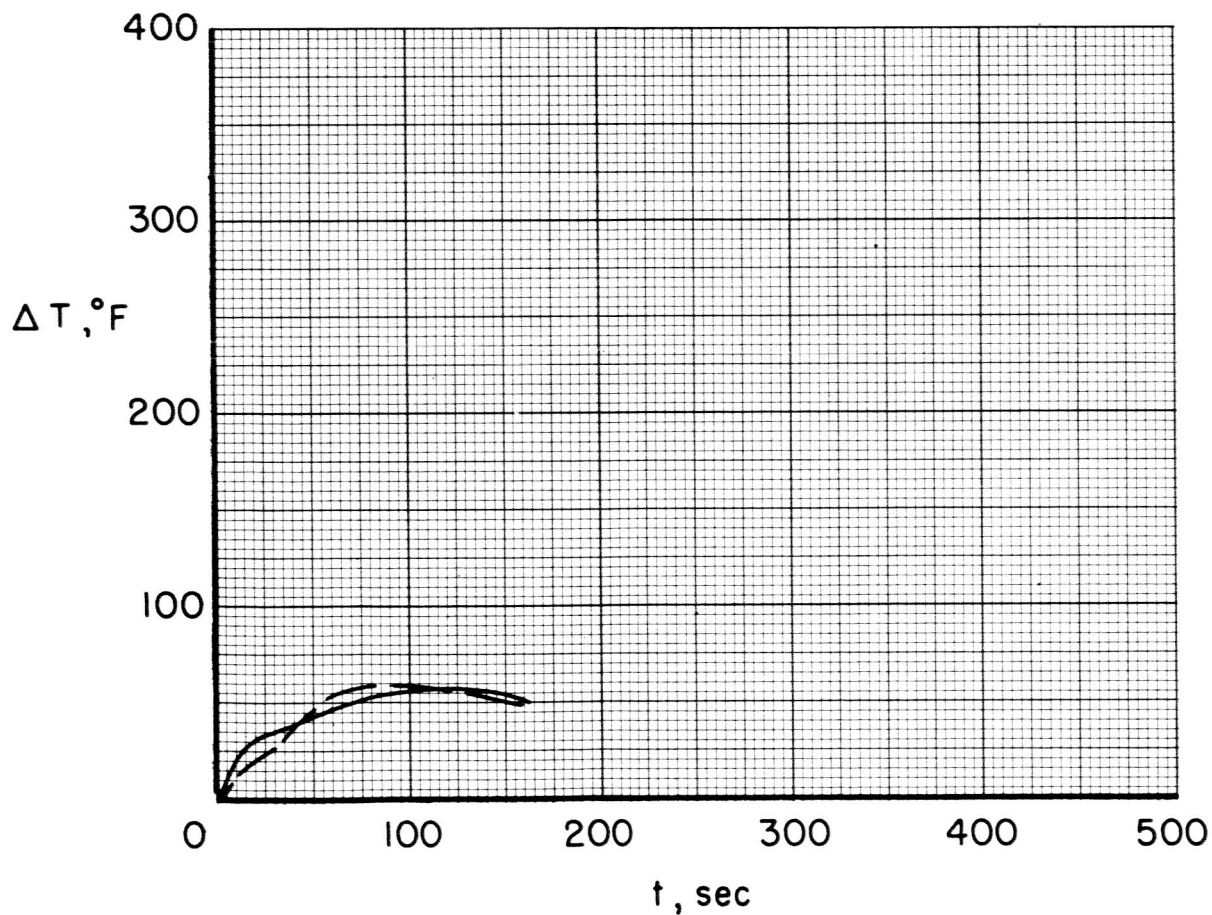
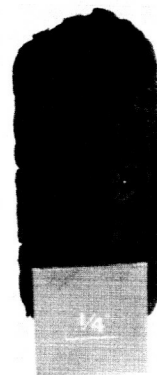


Figure 51.- Material number 44 (Balsa wood).

DECLASSIFIED

Composition

Insulating plaster

Density = 54 lb/ft³

Wt. Loss = 21 %

$\Delta T_{\max} = 53^{\circ}\text{F}$

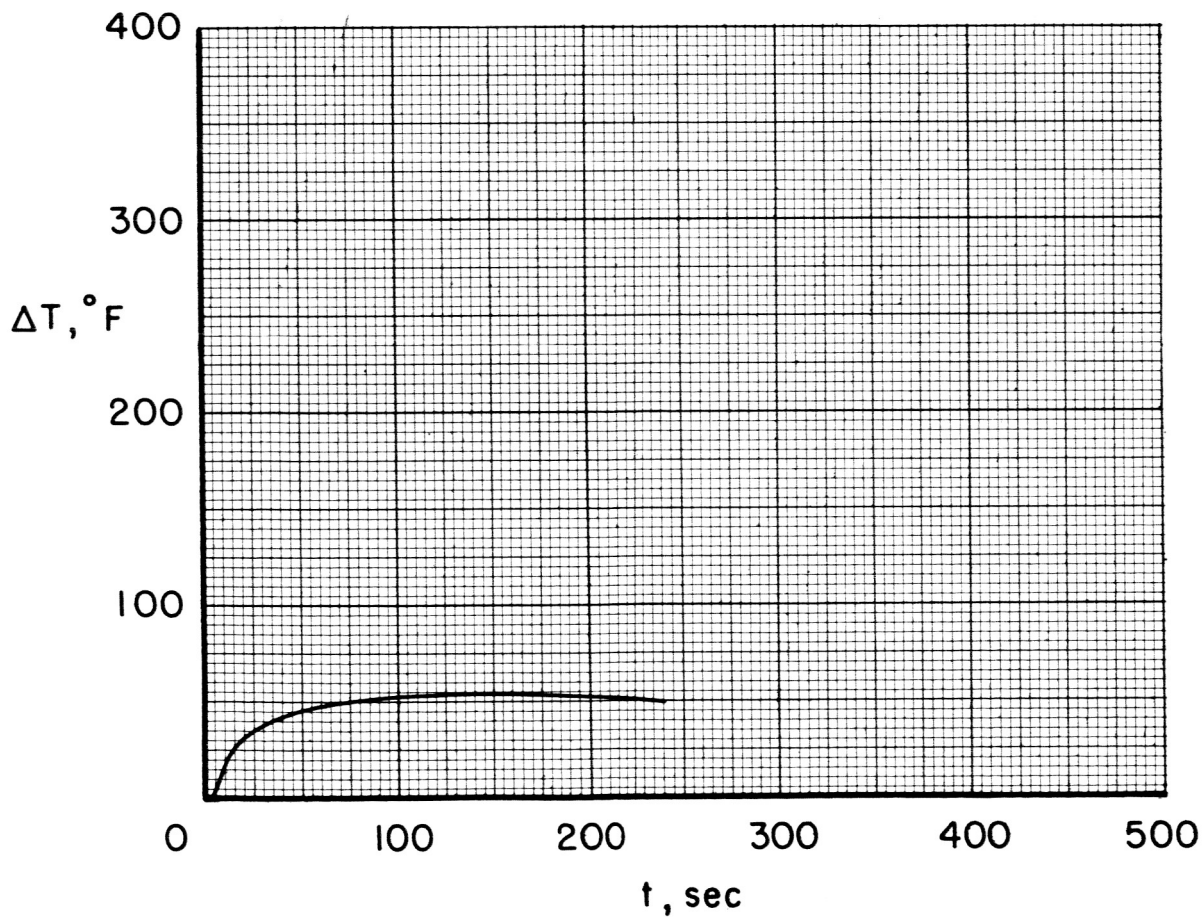


Figure 53.- Material number 46 (Vonolite).